6-2022

Investigating the Thermodynamics and Seismic Profile of the Europan Hydrosphere through Pure-Water Modeling and Saltwater Experiments

Samantha Rosenfeld
Union College - Schenectady, NY

Investigating the Thermodynamics and Seismic Profile of the Europan Hydrosphere through Pure-Water Modeling and Saltwater Experiments

By

Samantha L. Rosenfeld

****

Submitted in partial fulfillment

of the requirements for

Honors in the Department of Physics and Astronomy

UNION COLLEGE

June, 2022

ABSTRACT

ROSENFELD, SAMANTHA L. Investigating the Thermodynamics and Seismic Profile of the Europan Hydrosphere through Pure-Water Modeling and Saltwater Experiments. Department of Physics and Astronomy, June 2022.

ADVISOR: Dr. Heather C. Watson

We explore the properties of the hydrosphere on Europa involving both a modeling technique and experimental methods. We perform a computational analysis of the thermodynamic properties for an ideal, pure-water Europan ice shell using a Python programming framework called SeaFreeze. We create four models assuming surface temperatures of either 50 K or 140 K and ice shell thicknesses of either 3 km or 30 km. We observe mostly linear trends for the density and seismic wave velocities with respect to depth and find that surface temperature has the greatest effect on the models. Simultaneously, we experimentally investigate the phase diagram of different saltwater concentrations in an attempt to further constrain the ice shell properties. We determine the freezing temperatures of 5%, 10%, and 20% by-weight NaCl-water solutions under constant pressures from 0 MPa to 70 MPa. We find increasing the salt concentration, the pressure, or both decreases the freezing point temperature with a depression at our most extreme conditions of about -20 °C from that of pure water at zero pressure. Based on our experimental results, we expect that adding NaCl to the pure-water models would lower their ice-water boundary temperatures. Areas of future development include continuing to explore the phase diagrams of different saltwater concentrations, including MgSO4, KCl, and varying combinations of all three salts, extending the pure-water SeaFreeze models to analyze Europa's subsurface ocean layer, implementing various new techniques to make our experiments more precise, and finally applying our results to the other icy moons, such as Ganymede or Callisto.

Contents

List of Figures

List of Tables

1 Introduction

Life as we know it seems to be an anomaly. The probability of Earth being the only life-bearing planet in the entire Universe, when the Universe is so incomprehensibly large, seems extremely slim to none. Thus, we look to the skies to find the answer to one of the greatest questions of mankind: are we alone in the Universe?

1.1 Habitable Worlds

The search for life beyond Earth has never ceased since we discovered objects beyond our home planet. We analyze exoplanets and bodies within our own Solar System to see if they have the most basic and crucial building blocks for organisms to sprout. These bare necessities include whether the planet has organic molecular signatures and if it has the capability to maintain liquid water. In order for planets to sustain liquid water, they need to have some heat source to keep the water from freezing. This is why most astronomers who study exoplanets look for ones located in the Habitable or Goldilocks Zone, which is defined as the area around a star that has the right temperature conditions for water to be a liquid. In our Solar System, Earth is found within the Goldilocks Zone, thus allowing our planet to not be a frigid desert like Mars or a burning world like Venus (Kane and Gelino, 2012). However, there are other ways to generate heat on a planetary body, such as the process of tidal heating. Tidal heating is found as a heat source on moons that closely orbit much larger planets, where heat is generated by the friction created by differential gravitational forces. This heat source can be so strong that it keeps certain moons active, such as the violent volcanic eruptions on Io or the cryovolcanism on Enceladus. Due to this method of heating, we believe that some of the outer planets' icy moons may house liquid-water oceans under their icy surfaces, which could be hosts for life (Soderlund et al., 2020).

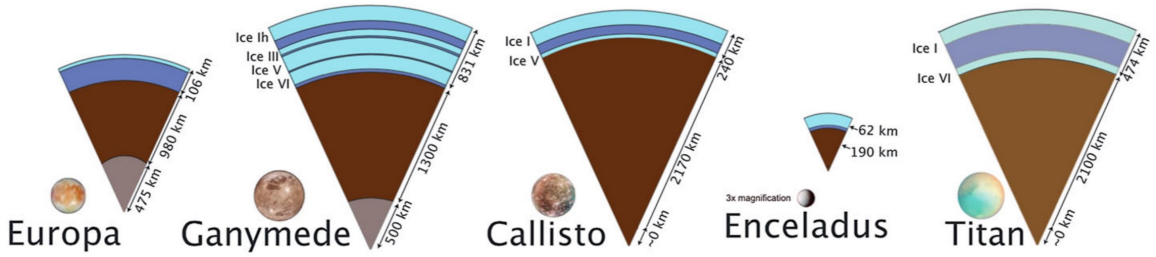

Figure 1: Theorized interior structure of Europa, Ganymede, Callisto, Enceladus, and Titan (Soderlund et al., 2020).

1.2 Inside the Icy Satellites

The icy moons of Jupiter and Saturn, such as Ganymede, Europa, Callisto, Titan, and Enceladus are the prime candidates for the search for life beyond Earth because of their theorized subsurface liquid water oceans. Figure 1 shows schematic diagrams of the interior structure of each moon that are based on data from both the *Galileo* (1989-2003) and *Cassini-Huygens* (1997-2017) missions to Jupiter and Saturn, respectively (Soderlund et al., 2020). Investigation into Ganymede through *Galileo* showed that it is composed of almost equal parts of silicate rock and water (Collins and Johnson, 2014). This is the same for Callisto, which really only differs from Ganymede in interior structure: Ganymede's interior is fully-differentiated, while Callisto's is not, meaning Ganymede has a rocky mantle and metallic core underneath its ice layers and Callisto has a core consisting of a mix of ice, rocks, and metal (Soderlund et al., 2020). Europa is known to be fully differentiated like Ganymede, except it is has a much a greater silicate rock to water ratio, where it is almost 8% water by mass (Ronnet et al., 2017). Enceladus is believed to also be differentiated, but with two layers: an ice shell, with a small local subsurface ocean, and porous rocky core. Finally, Titan, similar to Callisto, is believed to be only partly-differentiated. The three largest icy moons, and coincidentally the three largest moons in the Solar System, Ganymede, Titan, and Callisto, each have thick layers of H_2O that exist deep enough in their interiors to maintain high-pressure ices such as Ice II, Ice III, Ice V, and Ice VI (Soderlund et al., 2020). The Roman numerals for each ice type denote the different phase of ice. Ice I, or Ice Ih, is the most

Satellite	ρ (kg m^{-3})	R (km)	M (10^{22} kg)	e	T_{rot} (days)	$M_{silicate}$ (10^{22} kg)	% Ice by Mass	MoI Factor
Europa	2989	1565	4.800	0.010	3.55	4.459	7.1	0.346
Ganymede	1942	2631	14.819	0.0015	7.15	10.037	32.3	0.3115
Callisto	1835	2410	10.760	0.007	16.70	6.835	36.5	0.3549
Titan	1881	2575	13.453	0.029	15.95	8.799	34.6	0.34
Enceladus*	1608	252	0.0108	0.0047	1.37	0.0056	45	0.3305†

Table 1: Density (ρ), radius (R), mass (M), orbital eccentricity (e) about the parent planet, rotational period (T_{rot}), silicate mass ($M_{silicate}$), percent of ice by mass, and moment of inertia (MoI) factor for each icy ocean satellite. The data used for Europa, Ganymede, Callisto, and Titan is from Hussmann et al. (2015); *the data used for Enceladus is all from Schubert et al. (2007), †except for the MoI factor which is from McKinnon et al. (2015).

common phase of ice we naturally have on Earth.

These satellites' interiors have been determined through various observable and measurable characteristics including (1) radius, mass, and density, (2) gravitational field, (3) state and shape of rotation, (4) magnetic field, (5) heat flow and surface temperature, (6) surface and atmosphere composition, (7) surface activity, and (8) evolutionary history. Radius, mass, and density constrain the different compositions of the moons through our knowledge of the densities of common materials in our Solar System. For example, we know the density of Ice I is 920 kg m^{-3}, hydrated rock is about 2500 kg m^{-3}, nonhydrated silicate rock is approximately 3500 kg m^{-3}, and pure iron is approximately 8000 kg m^{-3}. Finding the densities of the icy moons, and using what we know about their radius and mass allows us to set a basis for different models to determine their interior compositions (Hussmann et al., 2015). Table 1 gives the known properties of the icy moons we are interested in, including density, radius, mass, orbital eccentricity about the parent planet, rotational period, silicate mass, percent of ice by mass, and moment of inertia (MoI) factor (Hussmann et al., 2015; McKinnon, 2015; Schubert et al., 2007).

We build off the baseline that is determined by the basic properties of these moons through data collected on them from recent missions. To measure the gravitational effects of these satellites, or any planetary object, close spacecraft fly-bys are needed to collect data on the gravitational

moments. These gravitational moments J_2 and C_{22} describe, respectively, the polar oblateness caused by rotation and the equatorial bulge caused by tidal interactions. Knowing these moments, it becomes feasible to determine the differentiation level of the planetary body. We can do this by finding whether the body has reached hydrostatic equilibrium, which is when the force of gravity produced by the amount of matter in the body and force of pressure produced by the compression of said matter attain equilibrium with each other. For hydrostatic equilibrium to be achieved, the body must satisfy the constraint in Equation 1.

$$J_2 = 10/3\, C_{22} \tag{1}$$

As an example, we have strong evidence that Io is in hydrostatic equilibrium because *Galileo* was able to measure each distinct gravity moment, and those measurements satisfy Equation 1. This gravitational data, when assuming hydrostatic equilibrium, can also be used to find the MoI factor using Equation 2,

$$\text{MoI} = \frac{C}{MR^2}\ , \quad \text{where} \quad C = \frac{8\pi}{3}\int_0^R \rho(r) r^4\, dr \tag{2}$$

where C is the moment of inertia, M is the mass of the body, R is the full radius of the body, and r is the radial distance from the center of the body (Hussmann et al., 2015).

The moment of inertia about the principal axes can also be determined through the body's rotational state; this is done without needing to assume hydrostatic equilibrium, but it can be more difficult because it requires precisely knowing the precession rate, which is the change in angular velocity and angular momentum due to torque applied by the rotation of the parent planet. This is a more complicated approach to determining the moment of inertia because precisely measuring precession takes long timescales. *Galileo* and *Cassini* both were equipped to measure the gravitational fields for each of the satellites, which determined the MoI factors and established whether hydrostatic equilibrium is achieved. However, *Galileo* could only distinguish the different gravity field moment measurements, J_2 and C_{22}, for Io, and not for the rest of the Galilean satellites (Hussmann et al., 2015).

1.3 Oceans and Heating Processes

The spacecraft missions to the two largest gas giants were very successful in finding evidence pertaining to subsurface liquid water oceans on their satellites. By measuring the magnetic fields of the moons, *Galileo* and *Cassini* provided the most convincing observational data for the existence of subsurface oceans. This is because Callisto, Europa, and (possibly) Ganymede have induced magnetic fields that are correlated with the variations in the principal Jovian field, which can be explained fully by the possible presence of salts in a liquid water layer located close to the surface. The ocean layers would need to contain some amount of salts in order to produce electrolytic conductivity, and thus create the induced magnetic fields. The magnitude of the induction response of the fields that the missions measured is proportional to the product of the electrical conductivity of the ocean and the ocean's thickness. This allows for salinity estimates to constrain the proposed thicknesses of the icy moons' oceans. An indirect way to detect these oceans can also be done through precisely measuring the tidal effects and gravitational field. This works because the tidal effects can vary based on the position of the moon in its orbit, namely through the difference due to when it is located at periapsis or apoapsis, the closest or farthest distance from the parent planet. These effects appear stronger if the satellite's orbit has a high eccentricity due to the large changes in its gravitational pull (Hussmann et al., 2015).

There are two distinctly well-known methods of heating that are widely established to exist in these moons: tidal heating and radioactive heating. Tidal heating is thought to be present in the icy moons discussed here and acts as the main energy resource for why these planetary bodies may be able to sustain liquid subsurface water oceans. It is most effective for satellites that either (a) are large in size, (b) have eccentric orbits, (c) are close to their primary planet, or (d) have high initial internal temperatures (leftover primordial heat). Among the Solar System satellites, Io, Europa, and Enceladus are the best satellites to meet the criteria for significant tidal heating, suggesting that this mechanism is responsible for the extreme volcanism and cryovolcanism of Io and Enceladus, respectively, and for the liquid-water interiors of Europa and Enceladus (Hussmann et al., 2015).

Radioactive heating processes are the transfer of heat due to the energy emission from long-lived radiogenic isotopes, which have half-lives of billions of years. To constrain the amount of radiogenic heating found in the icy moons, scientists determine the general amount of radioactive materials in their rocky compositions using the local chondritic composition found in that part of the Solar System (Hussmann et al., 2015). Chondrites are a type of asteroid that are widely used for dating the early Solar System (Kleine et al., 2002). The long-lived radiogenic isotope composition of chondrites includes uranium, thorium, and potassium, specifically ^{238}U, ^{235}U, ^{232}Th, and ^{40}K (Breuer and Moore, 2015). The heating rates of these radioactive decay processes are laboratory-derived through the measurement of the isotope half-lives and the energy released per individual-isotope decay. Neglecting short-lived isotopes that have mostly decayed a long time ago, these methods determined a specific present-day heating rate H to be on the order of several 10^{-12} W kg^{-1}, which is about one order of magnitude less than that theorized for the beginning of the Solar System (i.e., 4.6 billion years ago) (Hussmann et al., 2015). Thus, since radiogenic heating has become much less intense since the formation of these bodies, there must be some other source of heating that would allow for the existence of liquid water. We suspect tidal heating to account for the rest of the required heat.

If there exist oceans under the icy moons' surfaces, then there are many types of geophysical processes that could be occurring internally. Figure 2 shows a schematic diagram of the general interior of an icy moon hydrosphere that models different thermal and physical processes related to the distribution of brine (i.e., water highly concentrated with salt) and heat throughout the system. They suggest dense brine pockets can be formed from a concentrated brine mush layer along the ocean-mantle boundary. These pockets can be heated by the mantle and driven up through the ocean (or through a high-pressure ice layer to the ocean, in the case of Ganymede, Callisto, and Titan) via convection. The brine is then mixed throughout the ocean; brines close to the ice-ocean boundary could eventually be trapped in dikes within the ice shell, while brines within the ice shell could form "brinicles" or brine icicles that extend into the ocean. Deeper parts of the ice layer can also experience convection, which can bring brines near the surface, creating shallow subsurface

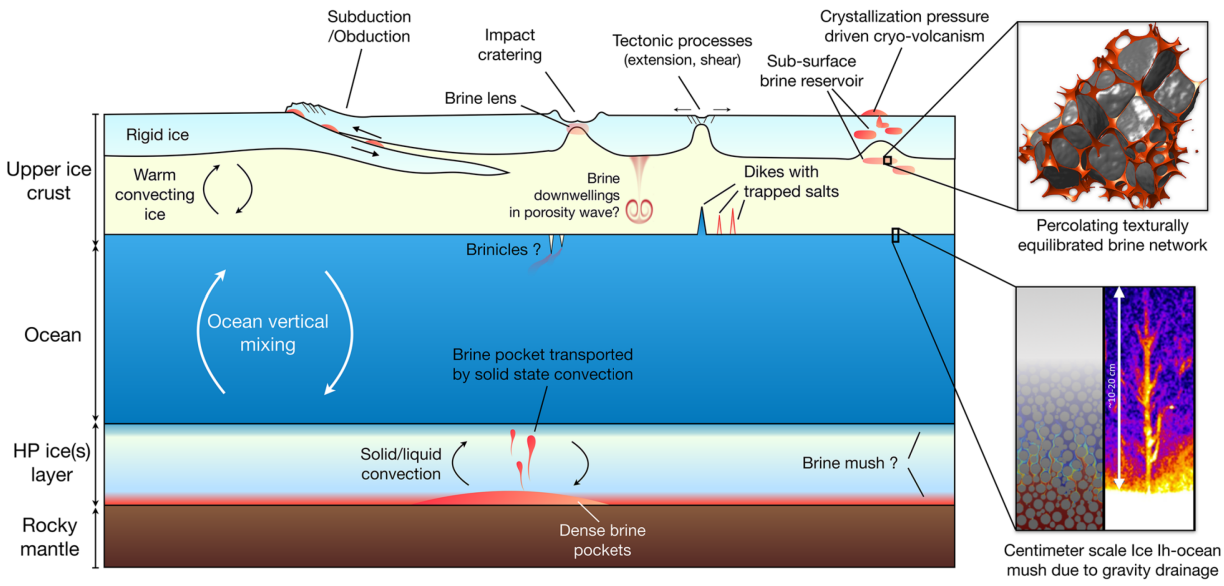

Figure 2: Schematic diagram of the ice shell and subsurface ocean, modeling the various geophysical processes that are possibly occurring under the surfaces of the icy moons. The high-pressure (HP) ice layer is only relevant to Ganymede, Callisto, and Titan (Vance et al., 2021).

brine reservoirs and lenses that could be exhumed by meteorite impacts, cryovolcanism, or tectonic processes like extension, subduction, or obduction (Vance et al., 2021).

The icy moons we focus on here are not only theoretically capable of holding liquid water, but they are also known to have some characteristics similar to Earth, which translate to further evidence of why they may be able to sustain life. In the case of the Saturnian satellite Enceladus, although it is tiny, scientists have already found organic compounds, ocean salts similar to those on Earth, silicate "nanograins," and evidence pertaining to hydrothermal activity all within a plume of materials ejected from the icy moon toward the *Cassini* spacecraft (Brennan, 2020). Titan is the only other planetary body in our Solar System that has rivers, lakes, and an entire hydrologic cycle like Earth; however, these features are predominantly composed of hydrocarbons, methane, and ethane—not water (Brennan, 2020). Despite the lack of surface water, Titan, like the other icy moons we discuss here, is believed to have a water ocean far beneath the surface. While Ganymede and Callisto both have evidence for salty liquid-water oceans, their oceans are believed to be sandwiched between thick layers of ice, which is not an ideal situation for the possibility of

the existence of life. Ideally, the ocean exists between the rocky mantle and ice shell, which is exactly Europa's situation (Brennan, 2020). Thus, we focus on Europa in our study because it is believed to have the greatest chance of hosting life compared to all of the other icy ocean worlds.

1.4 Europa

For our study, we are interested in Europa particularly due to the high possibility of its ocean being the next habitable entity outside of Earth. Using the methods described earlier for determining the differentiation-level, Europa is believed to be fully differentiated with an H_2O shell, a silicate mantle, and an iron-rich core. The most common density models assume Europa has a three-layer structure with a core ranging from 300 km to 700 km in radius, a water-ice layer that ranges between thicknesses of 80 km and 170 km, and a resulting silicate mantle that ranges between a thickness of 695 km and 1185 km. These estimates are dependent on the core and silicate densities, and if we assume hydrostatic equilibrium, the radii of the three layers can be calculated using the mass balance and moment of inertia equations shown in the system in Equation 3,

$$\begin{aligned} M &= \frac{4\pi}{3}\left[\rho_1 R_1^3 + \sum_{j=2}^{3} \rho_j \left(R_j^3 - R_{j-1}^3\right)\right] \\ \text{MoI} &= \frac{2}{5\rho R^5}\left[\rho_1 R_1^5 + \sum_{j=2}^{3} \rho_j \left(R_j^5 - R_{j-1}^5\right)\right] \end{aligned} \tag{3}$$

where each layer is designated by the iteration integer j (Hussmann et al., 2015). Magnetometer measurements from *Galileo* show Europa has a strong inductive magnetic field that is best described by an electrically conductive interior with an outer radius comparable in size to the entire radius of the Moon. However, there is no evidence pertaining to a permanent dipole, which, if Europa's ocean is greater than ten kilometers deep, can be explained by a water ocean similar in composition to the ocean found on Earth (Hussmann et al., 2015).

Europa's surface, as studied by *Galileo*, proves to be relatively young in age due to some

critical surface features. First, it contains a very small number of impact craters, which proves a drastic comparison to both Ganymede and Callisto's "ancient" surface features (Collins and Johnson, 2014; Hussmann et al., 2015). The small number of impact craters on Europa suggest that it has gone through recent resurfacing due to either tectonic or cryovolcanic processes, or both. Various models suggest that Europa's surface may be about ten million to several hundred million years old. Remaining surface features also are consistent with a surface age of several million years, which include specific tectonic features like chaos terrain.

There are several explanations and models for how chaos terrain may have been formed on Europa's surface. Here, we focus on a few of these possible theories; starting with the thin shell model, which suggests that if the ice shell is less than a few kilometers thick, then the surface must be in constant contact with the subsurface ocean because of tidal cracking and disruption (Greenberg et al., 1999). Another model suggests that the ice is broken by faults that are periodic due to tidal forces, which would expose the ocean and allow it to come up to the surface and refreeze. This process would also allow the surface to slowly shift as the ocean continues to be periodically uncovered in small amounts (Thomson and Delaney, 2001). There is also the potential for chaos terrain to be formed by what are called "liquid water lenses" that push up on the ice shell enough to crack it. This phenomenon would explain the large difference in topographic heights and depressions of the chaos terrain (Schmidt et al., 2011). Inspired by Io's internal processes due to extreme tidal heating, there is another model that suggests Europa's chaos terrain may be caused by volcanism at the mantle-ocean interface, where local heat sources that form in the silicate mantle travel up through the ocean and cause the surface to crack (Moore and Hussmann, 2009). Finally, subsurface ocean convection is one of the most widely accepted theories for chaos terrain and young surfaces on Europa. In this type of convection process, the hotter plumes of water would rise towards the surface, push up on the ice shell, cool off from the cold ice shell temperature, and then sink back down towards the mantle. The rising plumes could have enough force to crack the ice and freeze at the surface, causing the young surface features and chaos terrain that we observe, and they could sink to the bottom of the ocean and restart the convection process. This theory

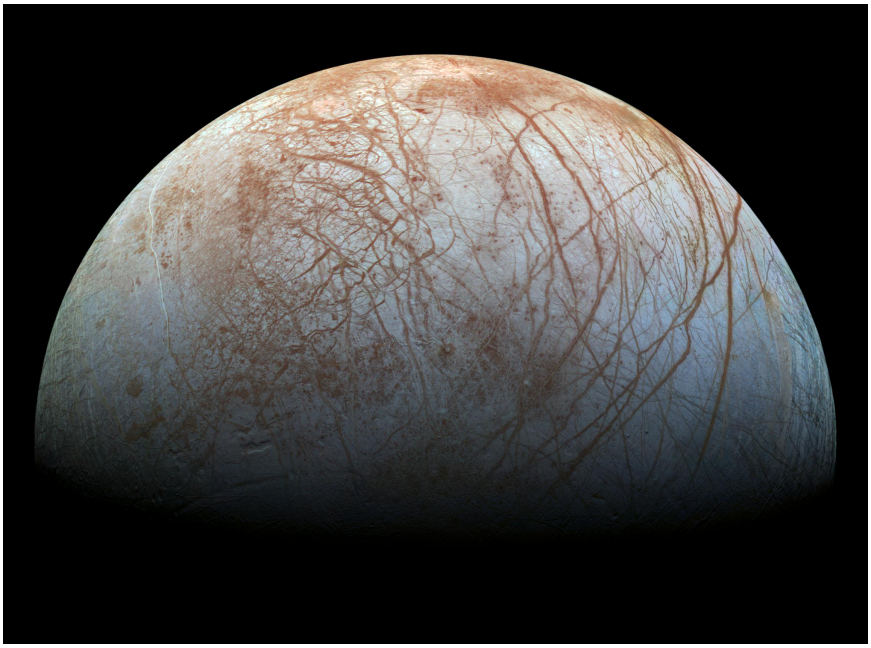

Figure 3: Color view of Europa, originally taken as a mosaic by *Galileo* in the late 1990s and published on November 21, 2014, by NASA/JPL-Caltech/SETI Institute. Image shows long cracks and chaos terrain that have been disrupted and refrozen over time (NASA et al., 2014).

would also be the most promising for astrobiology because similar conditions of ocean convection mixing occur on Earth (Lowell and DuBose, 2005). Our ocean regularly experiences convection both in the open ocean and under sea ice, which is crucial for regulating heat, carbon dioxide (CO_2), and nutrients for the various marine organisms and microorganisms to survive (Vreugdenhil and Gayen, 2021).

Chaos terrain and the long linear cracks on Europa's surface also provide strong evidence for tidal interactions. Hoppa et al. (1999) propose that when the tidal stress builds up in a specific area on Europa, due to its position relative to Jupiter, the forces can become so strong that it cracks the surface once the tensile strength of the ice is exceeded. The crack would propagate according to the tidal potential's time-varying stress field, which means that as time moves forward, the stress field changes and eventually causes the crack to stop if there is not enough tidal stress in the system. The cycle continues once the tidal stress builds up again; however, the crack would not be in the same place as before (due to a different stress field), and thus creates the crisscross pattern we observe on the surface (Hoppa et al., 1999). Figure 3 shows an image taken by *Galileo* that

displays these crossing cracks on the ice shell (NASA et al., 2014).

Another piece of evidence for the subsurface liquid ocean layer is called global decoupling. This is when a shell of some material "decouples," or behaves in a separate manner, to the rest of the body. We observe this for Europa's ice shell through *Galileo* data, where the rotation of the ice layer is suggested to be nonsynchronous on a timescale of about 10,000 years. Data suggests that it rotates at a slightly faster pace than the rest of the moon, indicating that the ice shell is decoupled from the rest of the moon, meaning there must be some layer that allows for it to act separately on a global scale. The only such layer that could make that possible is a liquid one. Thus, because we observe the ice shell to be globally decoupled, and we see an induced magnetic field that suggests some sort of electrolytic material, there must be a salty liquid water ocean underneath the ice shell (Hussmann et al., 2015).

While there exists very strong evidence for the existence of Europa's subsurface ocean, it still remains unconfirmed; this uncertainty drives the desire to return to the Jovian system, but this time to focus entirely on Europa. In the late 2020s, the National Aeronautics and Space Administration (NASA) is planning on sending a spacecraft science mission to Europa, called the Europa Clipper, which will conduct a detailed survey of the moon in order to determine if its conditions are suitable for life (see Figure 4 for an artist's rendition of the spacecraft near Europa). It seeks to study three important aspects of Europa: the ice shell and ocean, the composition and chemistry, and the geology. The payload for the Europa Clipper includes cameras and spectrometers for producing high-resolution images and maps, an ice-penetrating radar to search for a subsurface ocean, a magnetometer and gravity measurements to measure the magnetic field and understand Europa's interior, thermal instrumentation for pinpointing locations of warmer ice, and other instruments that measure the air particles in Europa's atmosphere. The Europa Clipper will also perform flyby observations of Ganymede and Callisto in between those of Europa, using the other two moons for correcting its orbit in the system (Pappalardo et al., 2021).

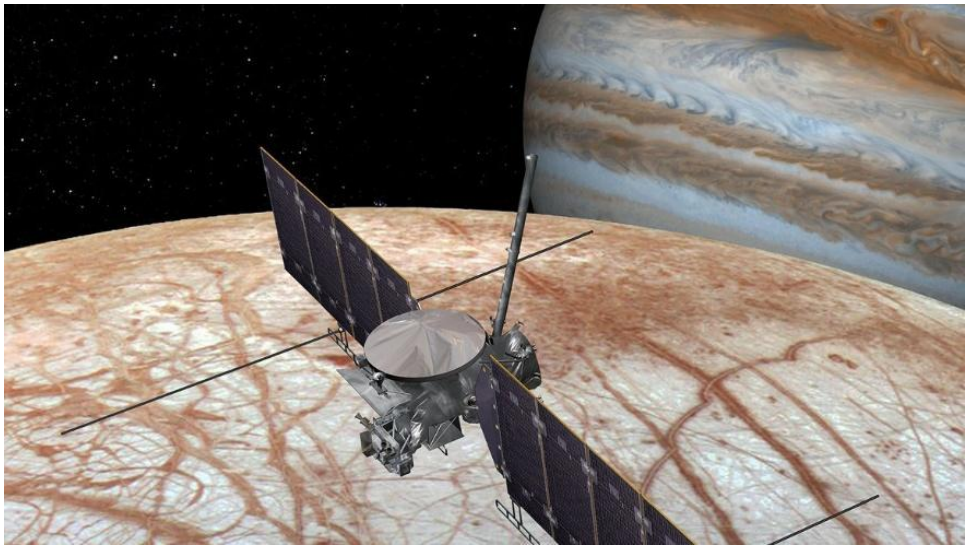

Figure 4: Artist rendition of NASA's Europa Clipper Mission near Europa and Jupiter (NASA and JPL-Caltech, 2016).

1.5 Our Focus

Since it will be some time before Europa Clipper can make its way out of our atmosphere, let alone to the Jovian system, we look to studying Europa's ice shell and subsurface ocean through performing a computational analysis of an ideal, pure-water Europan hydrosphere and experimentally investigating the phase diagram of different saltwater concentrations. We explore the density and seismic wave velocity profiles with respect to depth of an ideal ice shell using depths previously established as the possible Europan ice shell thicknesses. We can constrain the ice shell thickness and temperature gradient by comparing to the freezing point temperatures of various saltwaters at pressures relevant to Europa, using salts such as sodium chloride (NaCl), magnesium sulfate ($MgSO_4$), and potassium chloride (KCl). These comparisons are critical for constraining the ice shell's physical and thermodynamic properties. Section 2 presents the methods used for this study, where we first explore the ideal models before moving into our experiments. Section 3 details the results from our study, while Section 4 is where we make comparisons for our results and discuss the restrictions for the models and experiments. Finally, Section 5 concludes our study by summarizing our main findings and connecting them to future ice-ocean world exploration.

2 Methods

To begin our investigation into Europa's interior, we use both computational and experimental methods. We use computational modeling to understand the thermodynamic properties of pure-water ice at different depths, while the experiments look into how the freezing point changes if adding different salt concentrates. Together, the computational modeling and experimental results provide a more holistic view to us of what may be happening under Europa's surface.

Our experiments allow for a high precision analysis of the freezing points of different salt-water concentrations where we are able to get very precise measurements of pressure and temperature conditions at pressures that are directly relevant to the icy moons. Previous work through diamond anvil cell (DAC) experiments have only explored higher pressures that may be applicable to the ices found deep in Ganymede or Callisto, but are not applicable to Europa, Enceladus, or the ice shells found on the larger moons' surfaces. These DAC studies also result in large uncertainties in the temperature measurements on the order of about $\pm$ 5 °C to $\pm$ 27 °C that don't allow for detailed conclusions to be made in regards to the conditions on the icy moons (Frank et al., 2016). Our experiments both explore the lower and higher pressure conditions that are directly related to what we expect for Europa and the rest of the icy planetary bodies, and our experiments provide uncertainties of about $\pm$ 0.2 °C, which gives our study a unique level of accuracy as opposed to the rest of the field.

2.1 Computational Modeling

We use a Python program called SeaFreeze, a programming framework developed by Dr. Baptiste Journaux at the University of Washington. This program provides an environment in which to study the equilibrium thermodynamic properties of water for each phase extending into the metastable regime, including liquid water, Ice Ih, and some of the high-pressure ices (i.e., Ice

II, Ice III, Ice V, and Ice VI). The framework can calculate the thermodynamic properties of ice and water for ranges of pressure between 0 MPa and 2300 MPa and ranges of temperature between 200 K and 500 K, which makes it a useful tool when investigating high-pressure ices (Journaux et al., 2020). It is based on the Local Basis Function toolbox, developed by Dr. J. Michael Brown, which takes on a new approach for determining fluid dynamics through the use of "local basis functions," or b-splines. Through this development, Brown determined a modified equation of state for water, which determines the thermodynamic properties more accurately for our research purposes (Brown, 2018).

There are 18 thermodynamic properties that SeaFreeze calculates. The properties we focus on in this study are the material's density, primary wave (p-wave) velocity, secondary wave (s-wave) velocity, Gibbs free energy, shear modulus, and bulk sound speed. The density is the characteristic amount of mass of the material that fits within a certain volume. The primary or compressional p-wave and secondary or shear s-wave velocities are the velocities of seismic waves that either cause the material to move longitudinally (compressional waves) or laterally (shear waves). The Gibbs free energy is a measurement of energy referred to as the thermodynamic potential. It is minimized when a system reaches chemical equilibrium at constant pressure and temperature, and is the main driver behind why phase changes occur. Shear modulus describes the material's response to shear stress, or stress applied parallel to a material's cross-section. Bulk sound speed is the speed of sound within that material, which is a combination of the shear and compressional wave velocities and is dependent on the density of the material.

SeaFreeze not only calculates thermodynamic and seismic properties of water and ice as functions of pressure and temperature, but it can also determine the phase depending on the pressure and temperature given. Thus, we can use its output to plot the phase diagram of pure H_2O. Figure 5 shows an example of this, where if given a pressure range of 0 MPa to 1000 MPa and a temperature range of 220 K to 270 K, we can then see the phase boundaries between water and the different ices (Ih, II, III, V, and VI) (Journaux et al., 2020). We use this as a tool to figure out how

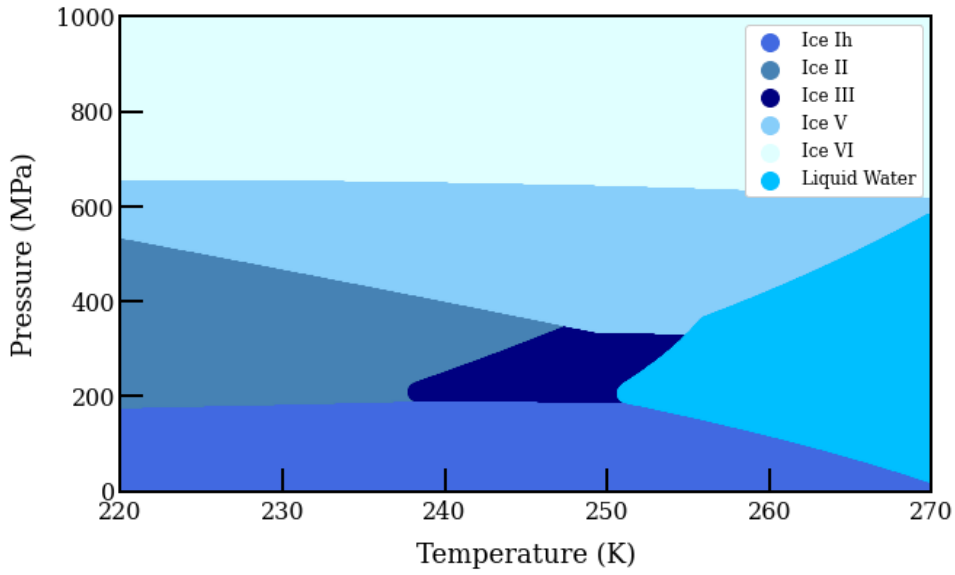

Figure 5: Phase diagram of pure water as calculated by SeaFreeze. The phases shown (in order from bottom to top, and from left to right) are Ice Ih, Ice II, Ice III, liquid water, Ice V, and Ice VI.

Ice Type	Pressure (MPa)		Temperature (K)	
	Low	High	Low	High
Ih	0	200	220	250
II	200	500	200	240
III	200	350	238	353
V	400	500	240	250
VI	680	1000	220	270

Table 2: Pressure and temperature boundaries for various ices.

best to analyze the plots of thermodynamic properties of water and ice and apply our results to the conditions on Europa. Table 2 gives the lower and upper boundaries of pressure and temperature used for each ice type in the SeaFreeze simulations. Since Ice Ih is the only known ice phase on Europa, we choose to focus on that specific phase. Appendix A shows the properties calculated for all of the phases of ice and Appendix B shows such properties across ice phase boundaries.

2.1.1 The Ice Shell

To apply our analysis of the high-pressure ices to the ice shell on Europa, we first determine the pressure and temperature conditions found for that layer. We do this through consulting the

literature, especially Soderlund et al. (2020), which gives calculated estimates based on data from previous spacecraft missions for the ice layer conditions. They give a range of 50 K to 140 K for the surface temperature, and they give an estimate for the ice layer thickness that ranges from 3 km to more than 30 km (Soderlund et al., 2020). Using these depth estimates, we find their corresponding pressures using Equation 4, which assumes that the depth that we analyze for the ice layer is small enough for the acceleration due to gravity g to stay constant.

$$P(h) = P_0 + \rho(h)gh \tag{4}$$

Where $P(h)$ is the pressure with respect to depth (h), P_0 is the atmospheric pressure, $\rho(h)$ is the density of the medium as a function of depth, and g is the acceleration due to gravity on Europa. At the surface, Europa's acceleration due to gravity is $g = 1.314$ m/s, which is about 13% of Earth's gravitational acceleration (Yeomans, 2006). Using Equation 4 and the depth estimates from Soderlund et al. (2020), we find that the pressure at the ice-water boundary should be some value between 3.6 MPa and 36.15 MPa (Soderlund et al., 2020). We next use these extreme values for the final ice layer pressures to find the corresponding melting-point temperatures that would allow for the existence of the ice-water boundary. We do this solely for Ice Ih because it is the ice type known to make up Europa's ice shell. Figure 6 shows two plots of Gibbs free energy at constant pressures as functions of temperature for Ice Ih (the green solid lines) and water (the blue dashed lines). We use pressures 3 MPa and 36 MPa for the two possible values at the ice-water boundary. The red dotted lines correspond to the intersection between the energy curves for Ice Ih and water, which tell us that the melting-freezing point of Ice Ih at 3 MPa is about 273.15 K, and that for Ice Ih at 36 MPa is about 270.999 K. We use these melting-freezing point temperatures with their corresponding pressures and the surface temperature range from Soderlund et al. (2020) to construct an array of temperatures and a range for pressure to plug into SeaFreeze in order to construct our models of Europa's ice shell (Soderlund et al., 2020).

Our first case uses a surface temperature of 50 K and an ice shell thickness of 3 km, trans-

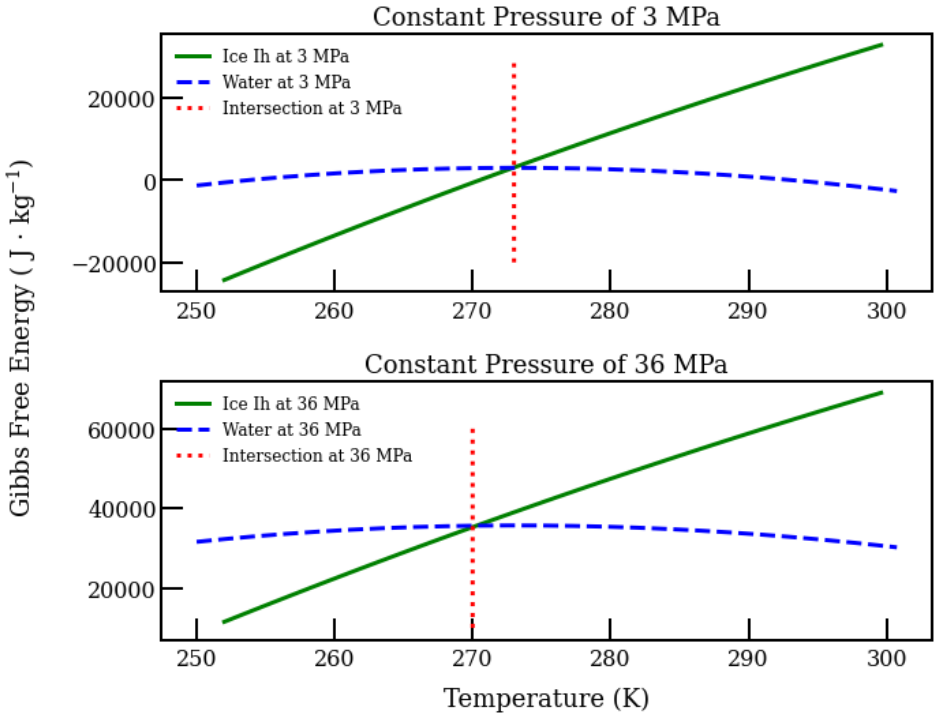

Figure 6: Plot of Gibbs free energy for Ice Ih (green solid lines) and liquid water (blue dashed lines) at constant pressure (3 MPa and 36 MPa) over a range of temperatures to determine the melting point temperature at the Ice Ih-water boundary. The red dotted line visualizes the intersection between the Ice Ih and water curves, depicting where the melting-freezing point temperature occurs.

Model Depth	Pressure (MPa)		Temperature (K)	
	Surface	Ice-Water Boundary	Surface	Ice-Water Boundary
3 km	0	3.6	50	273.15
3 km	0	3.6	140	273.15
30 km	0	36.15	50	270.999
30 km	0	36.15	140	270.999

Table 3: Surface and ice-water boundary pressure and temperature values used for ice shell models. We make arrays signifying the depth of the ice shell using these boundary values of pressure and temperature and input them into SeaFreeze to calculate the thermodynamic and seismic properties as functions of depth.

lating to a pressure at the bottom of the ice layer of 3.6 MPa. Our second case is exactly the same as the first, except it uses the higher surface temperature extreme value of 140 K. Our third case uses the lower extreme surface temperature of 50 K with an ice shell thickness of 30 km, which makes the pressure at the bottom of the ice shell about 36.15 MPa. Similar to the difference in the first two models, our fourth case follows the same conditions as the third model except for the surface temperature, for which we use the higher boundary of 140 K. Table 3 gives the boundary values for the temperature and pressure used in each of the ice shell models.

To input our models into SeaFreeze for computing the thermodynamic and seismic properties, we create arrays of pressure and temperature using the boundary values that vary between each model. We also assume a linear temperature gradient with depth, which may not be the exact temperature distribution as that of Europa's ice shell, but it provides an ideal starting point that we can work from as we develop our models further in the future. For an ice shell thickness of 3 km, we make two temperature arrays to each be 100 values that range from either surface temperature (50 K or 140 K) to 273.15 K. The pressure arrays used for these models are the same because they assume the same ice shell thickness of 3 km, which means our pressure array becomes a range of 100 values between 0 MPa and 3.6 MPa. For the ice shell thickness of 30 km, we make two more temperature arrays with 100 values each ranging between either surface temperature (50 K or 140 K) to 270.999 K. We make the pressure arrays for both of our models using a 30 km depth as the same pressure array due to them assuming the same depth value, which means we create one pres-

sure array of 100 values between 0 MPa and 36.15 MPa for these two models. Next, we calculate each model's thermodynamic and seismic properties as functions of temperature and pressure by plugging in their respective arrays to SeaFreeze. We do this to analyze some of the thermodynamics properties of Ice Ih under Europan conditions, looking at density, p-wave velocity, s-wave velocity, Gibbs free energy, shear modulus, and bulk sound speed (results shown in Section 3.1.1). Then, we choose to focus on density, p-wave velocity, and s-wave velocity for our models of the ice layer with respect to depth (results shown in Section 3.1.2).

2.2 Saltwater Freezing Point Experiments

To investigate the phase diagram of different saltwater solutions at varying pressures, we use a freezing tank, a high-pressure vessel, a pressure pump system, and two temperature sensors in our experimental apparatus. Figure 7 shows an image of the experimental apparatus while Figure 8 shows an enlarged view of the freeze tank. The freeze tank (labeled with the white bracket in Figure 7) is the large box located in the lower left corner, which is covered with a reinforced plastic shield both to protect researchers from any potential malfunctions with the pressure vessel and to keep dust and other interfering particles and objects away from the anti-freeze bath (colored green). One of the ways we measure temperature is through the external temperature probe, labeled in cyan in Figures 7 and 8, where its temperature sensor is placed inside the anti-freeze bath directly next to the pressure vessel that contains the sample. The pressure vessel (labeled in orange in Figures 7 and 8) is submerged in the anti-freeze bath, and it contains our second temperature probe, which is a resistance temperature detector (RTD) temperature sensor or thermocouple device that directly measures the resistance of the sample, as it is secured within the pressure vessel's chamber. The pressure screw-pump system, labeled in red in Figures 7 and 8, connects to the other side of the pressure vessel (the side opposite the thermocouple) via thin tubes. The screw-pump is the long piece of tubing that has a large wheel on its end; we turn the large wheel counter-clockwise to tighten the screw-pump and thus increase the pressure, and we turn it clockwise to loosen the

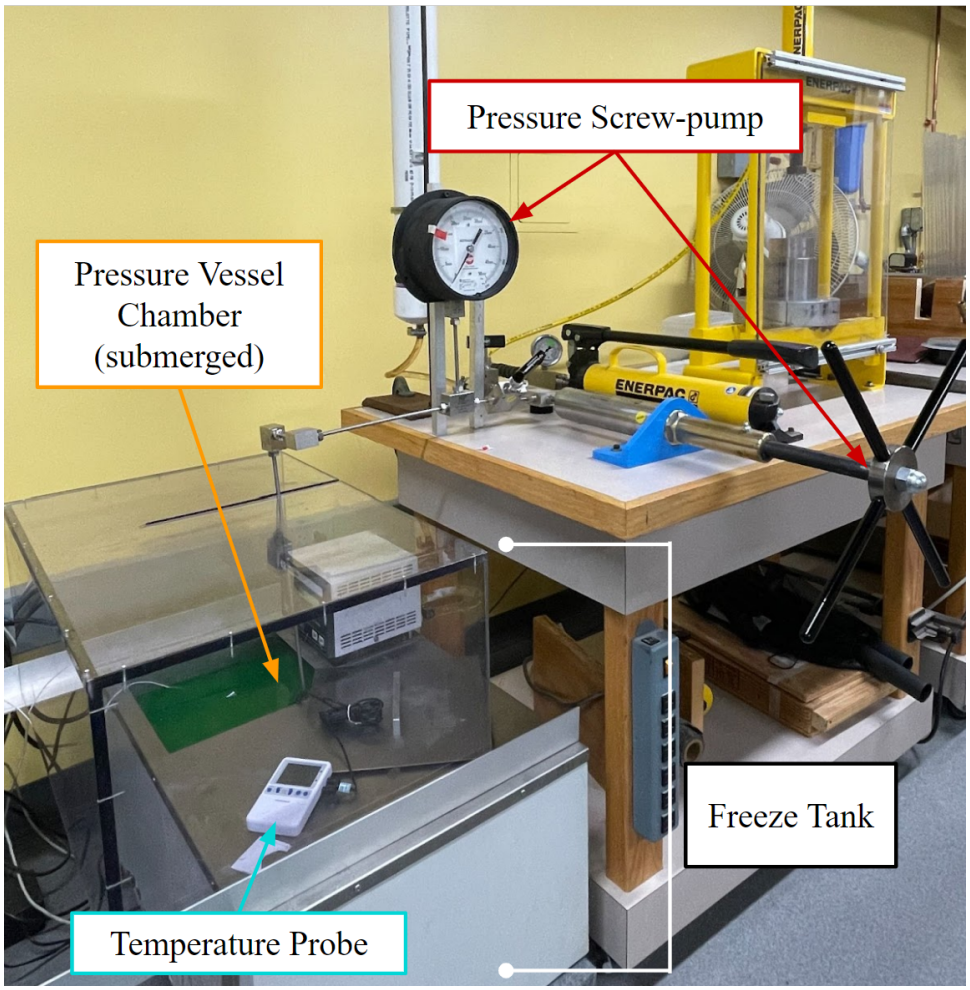

Figure 7: The full set-up of our freezing experiment, where the freezing tank (white bracket) is located in the bottom left of the image, which contains the anti-freeze bath; the external temperature probe (cyan arrow) is placed inside the anti-freeze bath directly next to the pressure vessel (orange arrow); finally, the pressure screw-pump system (red arrows) is connected to the pressure vessel through a tubing system.

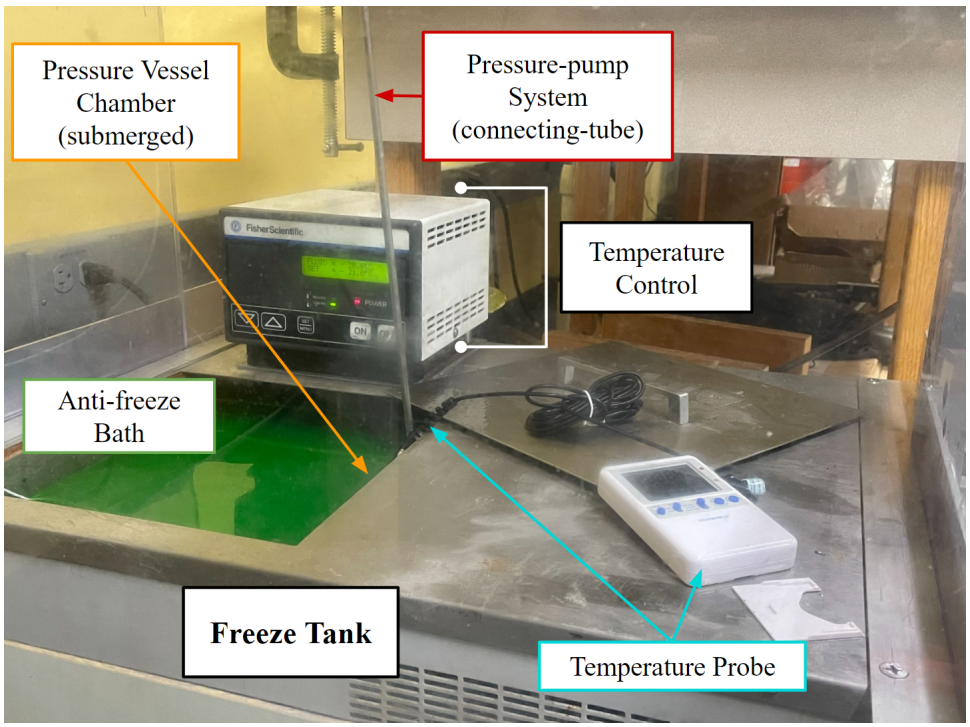

Figure 8: An enlarged view of the freezing tank: the tank contains the anti-freeze bath (colored green), the external temperature probe (cyan arrows) is placed inside the anti-freeze bath directly next to the pressure vessel (orange arrow), and the pressure screw-pump system (red arrow) is connected to the pressure vessel through a tubing system. There is also the temperature control system (white bracket) connected to the tank that allows us to set the temperature of the bath.

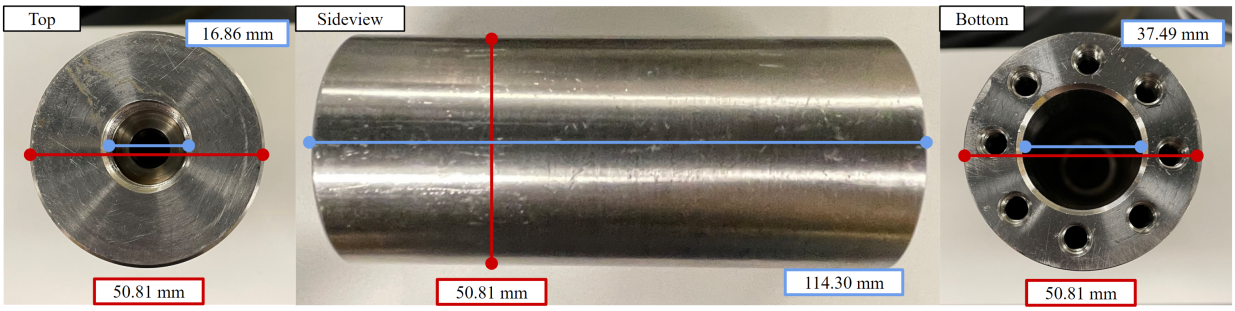

Figure 9: The pressure vessel tube shown from the top (left panel), side (middle panel), and bottom (right panel) with various dimensions in blue and red.

screw-pump and thus decrease the pressure. The pressure screw-pump system has an associated uncertainty of about 250 pounds per square inch (PSI), which is approximately 1.72 megapascals (MPa). This small uncertainty allows us to investigate the freezing points of our samples within a very precise range of constant pressures. Since the pressure gauge measures in PSI, we choose our constant pressure values to be 0 PSI, 2500 PSI, 5000 PSI, 7500 PSI, and 10,000 PSI, which corresponds to 0.00 MPa, 17.24 MPa, 34.47 MPa, 51.71 MPa, and 68.95 MPa, respectively. We will be referencing these pressure values in megapascals for the rest of this report.

The pressure vessel has a few distinct parts that make it an excellent chamber for the samples in our freezing experiments. Figures 9-12 show the various parts that make-up the pressure vessel along with their dimensions. Figure 9 shows the tube that makes up most of the vessel, with the top shown on the left panel, sideview on the middle panel, and bottom on the right panel. The small piston, shown in Figure 10 fits into the pressure vessel tube through the bottom of the tube (with the small piston's top-side facing in the same direction as the bottom of the vessel tube; i.e., the top of the small piston faces the outside of the pressure vessel tube based on how it is inserted into the bottom of the tube). Not shown is the bottom of the small piston, which is just a flat surface. The piston cap, shown in Figure 11, also fits into the bottom of the vessel tube and is the part that connects the pressure screw-pump system to the pressure vessel, via the piston mechanism. The other side of the tube (i.e., the top shown in Figure 9), is where the RTD thermocouple (Figure 12) fits into the pressure vessel. The RTD thermocouple has three main components: (1) the RTD

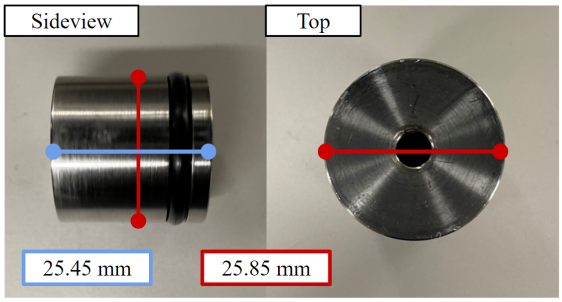

Figure 10: The small piston that can be inserted inside the pressure vessel tube (from the bottom) shown from the side (left panel) and top (right panel) with dimensions in blue.

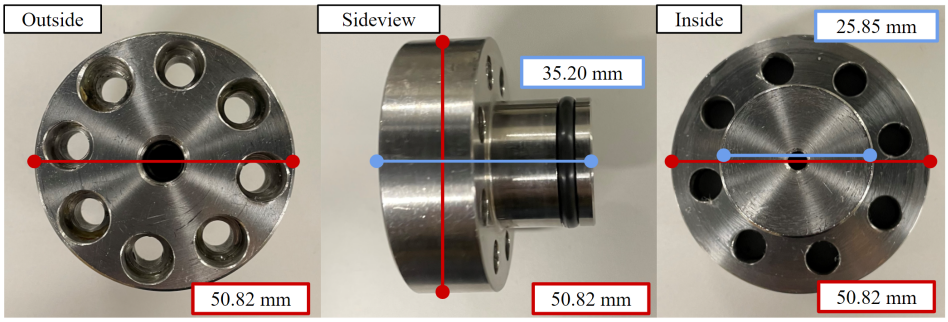

Figure 11: The pressure vessel piston cap that can be inserted into the bottom of the pressure vessel tube is shown from the outside (left panel), side (middle panel), and inside (right panel) with various dimensions in blue and red.

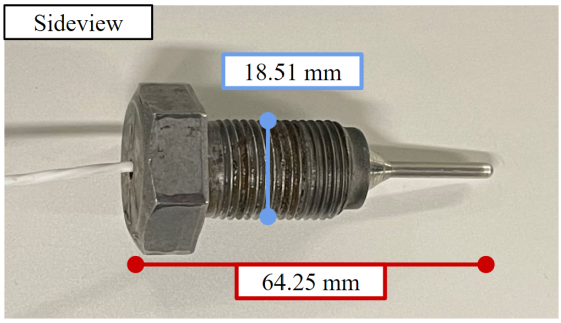

Figure 12: The resistance temperature detector (RTD) thermocouple, which can be screwed into the top of the pressure vessel tube, is shown from the side with dimensions in red and blue.

temperature sensor, which is the shiny probe that is located on the far right side in Figure 12, (2) the screw-head, which is what allows us to fit the RTD thermocouple in the pressure vessel to be immersed in the sample, and (3) the RTD temperature sensor's wire, which follows from the RTD sensor, through the screw-head, and out of the pressure vessel to carry the resistance and temperature information measured from within the sample to a digital multimeter so that we can record our data.

We use approximately 20 mL of the sample in each of the freezing experiments, which is a solution of distilled water and a high-purity solute with a concentration of 5%, 10%, or 20% by weight. For our purposes, we investigate different concentrations of sodium chloride (NaCl) with water. We calculate the amount of solute needed per concentration using the formula shown in Equation 5 (assuming the density of water is approximately 1 g mL^{-1}),

$$m_{\text{solute}} = \frac{(\%\text{ weight concentration})(V_{\mathrm{H_2O}})}{100 - (\%\text{ weight concentration})} \tag{5}$$

where m_{solute} is the mass of the solute used, % weight concentration is the percent weight concentration of the solute to the water (e.g., 5 for 5%, 10 for 10%, or 20 for 20%), and $V_{\mathrm{H_2O}}$ is the volume of solvent or distilled water. We use Equation 5 to find the amounts of solute we need per sample, which we make in batches of about 100 mL each. Using 100 mL of distilled water, we stir in approximately 5.26 g of high-purity NaCl for the 5% samples. Similarly for the 10% and 20%

solutions, we mix 100 mL of distilled water with 11.11 g and 25.00 g of NaCl for each respective solution. We perform our freezing-point experiments by starting with the 5% concentration solution under varying pressure conditions, then repeat the trials using the same varying pressures with each of the higher-level concentrations (i.e., study 10%, then 20%).

Before we can fill the pressure vessel with the sample, we first secure it in a large clamp to keep it in place, and thoroughly clean all of its pieces using distilled water and ethanol. Then, we place the small piston (Figure 10) into the bottom of the pressure vessel cylinder (which is the right panel of Figure 9), and use the piston cap (Figure 11) to push the small piston inside. We then use screws to secure the piston cap to the cylinder, ensuring the cap is secured evenly across the pressure vessel by tightening each screw in a crisscross pattern. Then, after turning the cylinder such that the open part of the vessel faces up, which is the top of the tube shown in Figure 9, we fill a syringe with the NaCl-water solution and use it to place approximately 20 mL of the sample into the vessel. Finally, once the sample is in place, we screw the RTD thermocouple (Figure 12) into the top of the pressure vessel cylinder, using a wrench to keep it closed tight and a small amount of Marine-Grade Bostik Never Seez NMCBT-16 to ensure the pressure vessel is water-tight.

We immerse our pressure-vessel filled with the sample into the anti-freeze bath, which is in a tank connected to a temperature control system that allows us to cool the sample at low temperatures. By immersing the vessel into the bath, we also connect it to the pressure-pump system which allows us to accurately set the pressure inside the vessel. We finally also connect the thermocouple to an Agilent 34401A 6 1/2 digit multimeter to measure the resistance, which we also connect to the computer for automatically logging the resistance of the sample. The data collection software we use to record the resistance throughout the experiments is the Keysight PathWave BenchVue Software. We use two additional temperature probes: one probe within the anti-freeze bath itself to keep track of the temperature outside of the pressure-vessel, and another built-in to the freeze-tank to tell us what the temperature control system reads as the current bath temperature.

Turning the tank on starts a circulating process that continuously stirs the anti-freeze to ensure the entire tank volume cools at the same rate. After the vessel is in thermal equilibrium with the bath, we use the temperature control system on the tank to set the temperature to a few degrees Celsius lower than the anticipated freezing point. This allows the sample to undercool, which proves to be advantageous for our particular analysis because it allows us to determine the freezing point temperature to high precision by taking the peak value of our data (example curve shown in Figure 13). Undercooling is when a liquid attains a temperature below its melting-freezing point but does not freeze. Once it reaches a few degrees below the freezing point, either it begins to freeze on its own or we toggle the freezing process by quickly increasing and decreasing the pressure around the set pressure at which we are analyzing the sample. While saltwater freezes, it characteristically increases in pressure; thus, to keep it under constant pressure, we periodically adjust the pressure system to our initial set pressure. Once we observe the end of the freezing process, we allow it to cool down to the original undercooling temperature, and later heat the system back up to 0 °C. Figure 13 shows an example of the freezing curve for one of the experiment trials, which used the 20% NaCl sample at a constant pressure of 0 MPa. We are able to toggle the freezing process using the pressure screw-pump system, which influences the resistance and consequently temperature to produce the small spikes near the base of the curve in Figure 13. Alternatively, for most of the lower salinity samples, the freezing process begins without needing to change the pressure. Once freezing, the sample releases latent heat which drives the temperature up until it plateaus at the freezing/melting point, and then continues to cool once the entire sample is frozen. This process of undercooling, to latent heat release, to freezing, to cooling again is what forms the peak in Figure 13. We determine the freezing point for the trial by taking the peak temperature of the freezing curve, which, as was mentioned before, is advantageous because it allows us to find the freezing temperatures to high precision. We repeat this process several times for each sample with 5%, 10%, and 20% salt concentrations by weight under 0 MPa, 17.24 MPa, 34.47 MPa, 51.71 MPa, and 68.95 MPa pressure conditions (results shown in Section 3.2).

Finally, it is important to note that there has been ongoing work on the calibration of the

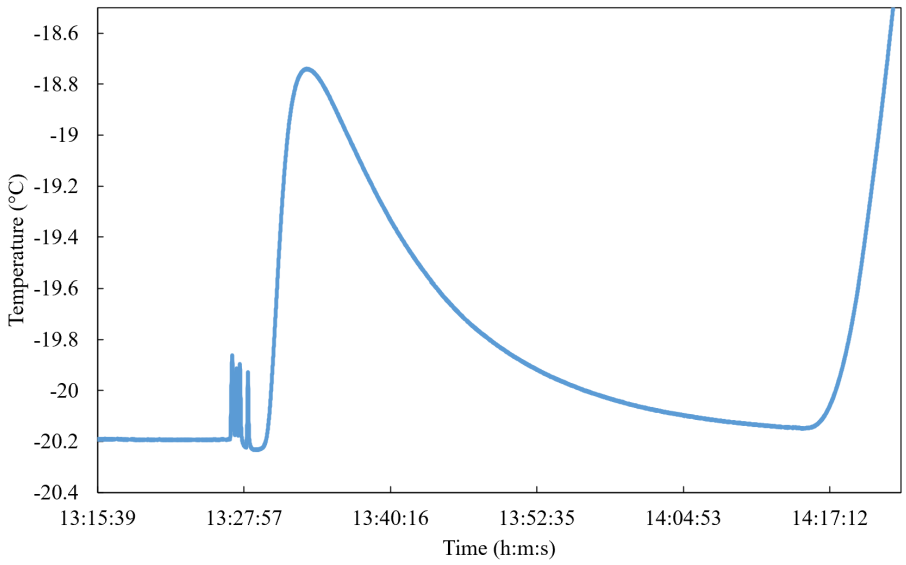

Figure 13: An example freezing curve of one of the trials that used the NaCl 20% concentration sample under a constant pressure of 0.00 MPa $\pm$ 1.72 MPa (also shown in Figure 24 in Section 3.2). The y-axis shows the temperature of the sample in Celcius, and the x-axis shows the time of day the experiment was performed in hours, minutes, and seconds; this trial was done on October 15, 2021. The freezing point for the sample is found at the peak, which is evaluated to be -18.75 °C $\pm$ 0.26 °C for this particular example.

RTD sensor. The calibration would provide us with the ability to make any minor corrections in the saltwater freezing point temperature experiments, making our results even more accurate. Currently, the calibration has not yet been applied to the results. Regardless, our results are both more accurate and precise than previous work, particularly because there are no known data for the freezing temperature of the NaCl solution over the pressure range that we probe, except for at atmospheric pressure, which is about 10 MPa.

3 Results

We now outline the results of both the computational modeling of the ice shell and the saltwater freezing point analysis experiments.

3.1 Computational Modeling

Using SeaFreeze to calculate the thermodynamic and seismic properties of pure-water ice allows us to plot the resulting thermodynamic properties as functions of depth. We first investigate each individual property and its relationship to different pressure and temperature conditions relevant to Europa. We then narrow our focus on the density, p-wave velocity, and s-wave velocity under four varying pressure-temperature conditions that represent the various possible conditions of Europa's ice shell.

3.1.1 Thermodynamic Properties of Ice Ih

We first look at each thermodynamic and seismic property as functions of pressure and temperature (i.e., depth) for Ice Ih using contour plots. The properties we investigate here include density, p-wave velocity, s-wave velocity, Gibbs free energy, shear modulus, and bulk sound speed. Figures 14-19 show the calculated results for these properties in their respective order. Within Figures 14-19, each plot on the left side is for a depth of 3 km while each plot on the right side is for a depth of 30 km, which are the two extreme estimated thicknesses for Europa's ice shell. The 3 km depths use an array of pressures ranging from 0 MPa to 3.6 MPa and temperatures from 50 K to 273.15 K, while the 30 km depths use pressures from 0 MPa to 36.15 MPa and temperatures from 50 K to 270.999 K.

In Figure 14, for the ice-water boundary pressure of 3.6 MPa, the density tends to decrease

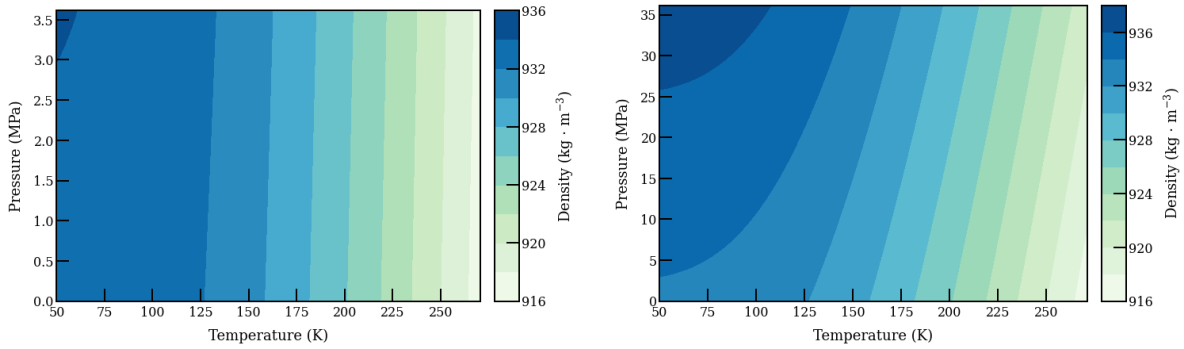

Figure 14: Density gradients for Ice Ih plotted as functions of temperature and pressure with an ice shell boundary pressure of (left) 3.6 MPa and (right) 36.15 MPa. The density increases from a light green to a dark blue. We find the density increases at a faster rate at lower temperatures under high pressure but increases linearly with decreasing temperature, otherwise.

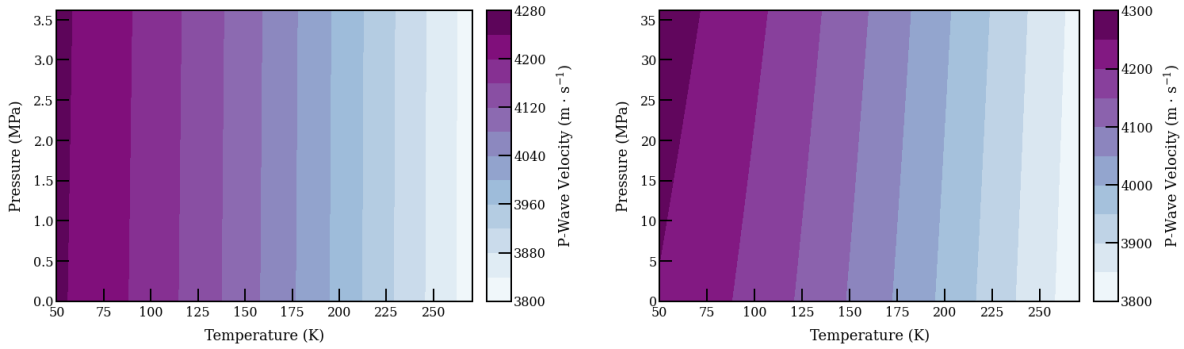

Figure 15: Primary wave velocity gradients for Ice Ih plotted as functions of temperature and pressure with an ice shell boundary pressure of (left) 3.6 MPa and (right) 36.15 MPa. The p-wave velocity increases from a light blue to a dark violet. We find the p-wave velocity decreases linearly with increasing temperature and is constant with changing pressure.

linearly with increasing temperature and stays constant across changes in pressure. However, at higher pressures (i.e., for the plot that uses an ice-water boundary pressure of 36.15 MPa) the density tends to slowly increase with higher pressure values while also decreasing with increasing temperature. This produces a contour that resembles a parabolic distribution at high pressures and low temperatures.

The seismic wave velocities seem to be much less affected by pressure than the density. Figure 15 shows the p-wave velocity contours with respect to pressure and temperature. The p-wave velocity seems to decrease with increasing temperature and stay constant with changing

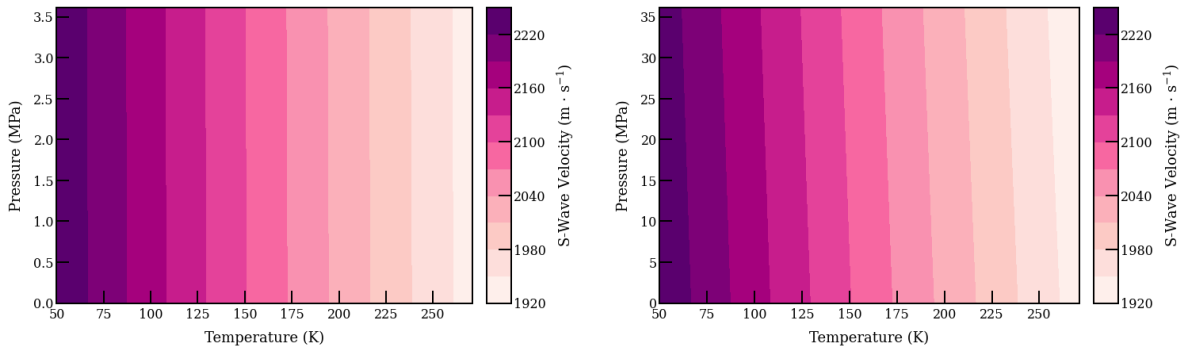

Figure 16: Secondary wave velocity gradients for Ice Ih plotted as functions of temperature and pressure with an ice shell boundary pressure of (left) 3.6 MPa and (right) 36.15 MPa. The s-wave velocity increases from a light pink to a dark violet. We find the s-wave velocity decreases linearly with increasing temperature and is relatively constant with changing pressure.

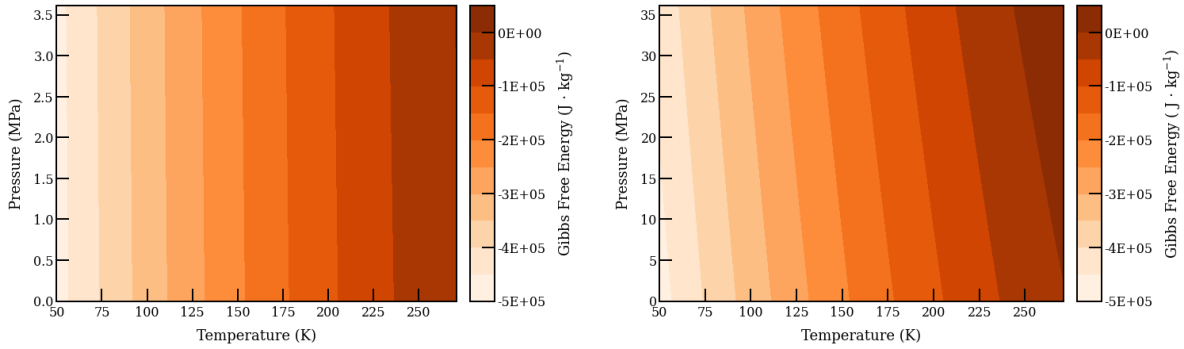

Figure 17: Gibbs free energy gradients for Ice Ih plotted as functions of temperature and pressure with an ice shell boundary pressure of (left) 3.6 MPa and (right) 36.15 MPa. The Gibbs free energy increases from a light orange to a dark orange. We find the the Gibbs free energy increases linearly with decreasing temperature and is relatively constant with changing pressure.

pressure for both of the different boundary pressure cases. However, there is a slight change in the contour slopes for the higher pressure case, which shows that the higher pressure values cause the p-wave velocity to experience a slight increase. The s-wave velocity contours, shown in Figure 16, also seem to have a very consistent relationship with the given pressure and temperatures, where the s-wave velocity decreases linearly with increasing temperature and stays constant over the range of pressures. The only difference is that for the higher boundary pressure case, the s-wave velocity experiences a slight decrease at higher pressures.

The contour plots for Gibbs free energy are given in Figure 17, where the energy values

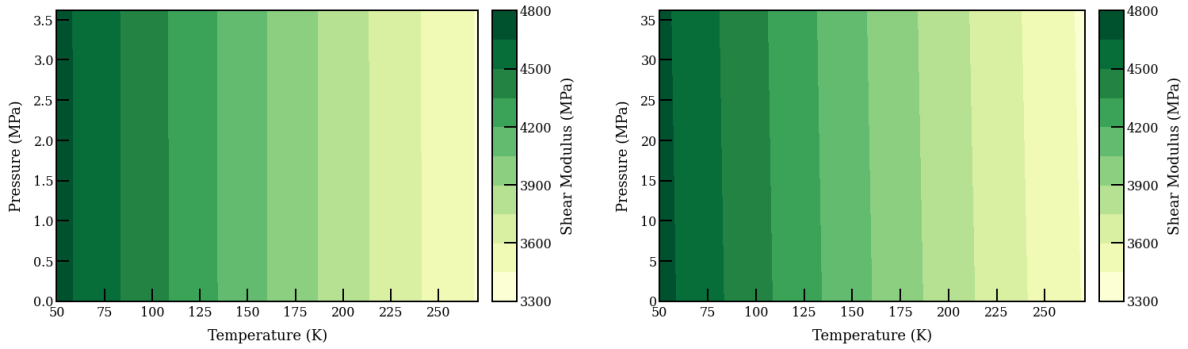

Figure 18: Shear modulus gradients for Ice Ih plotted as functions of temperature and pressure with an ice shell boundary pressure of (left) 3.6 MPa and (right) 36.15 MPa. The shear modulus increases from a light green to a dark green. We find the the shear modulus decreases linearly with increasing temperature and is constant with changing pressure.

experience an opposite effect than the rest of the properties with respect to temperature. The Gibbs free energy increases with increasing temperature, and actually becomes more negative in value at lower temperatures. This result is consistent with how Gibbs free energy is the main parameter that dictates the phase changes in materials, where the phase change occurs because it would be more energetically favorable (i.e., the Gibbs free energy would be lower) for the material to be in a different state. Since we are analyzing only Ice Ih up to its melting conditions at the ice-water boundary, it follows that the Gibbs free energy approaches a higher value closer to the boundary, and a much lower value away from it. Additionally, the Gibbs free energy does stay constant with changing pressure for the lower boundary pressure case, similar to the rest of the properties, but it seems to increase slightly at higher pressures for the higher boundary pressure case.

The shear modulus in Figure 18 seems to share the same pattern under lower pressures as most of the other properties, which is that of having a constant value with changing pressure and linear decrease with increasing temperature. The shear modulus is unique, however, because it has this consistent pattern for both of the different boundary pressure cases. This means that because the shear modulus is the ratio of shear stress to shear strain, either the shear stress decreases or the shear strain increases with increasing temperature, while their ratio stays the same under varying pressure at constant temperature.

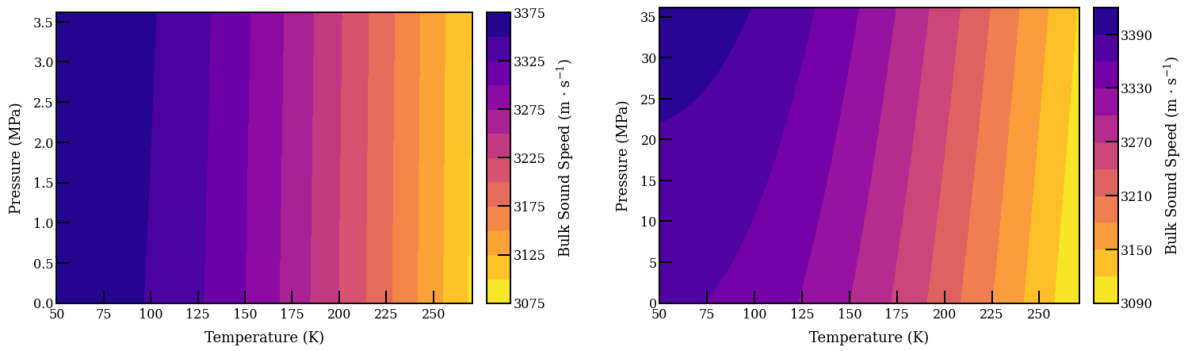

Figure 19: Bulk sound speed gradients for Ice Ih plotted as functions of temperature and pressure with an ice shell boundary pressure of (left) 3.6 MPa and (right) 36.15 MPa. The bulk sound speed increases from a bright yellow to a dark purple. Similar to density, the bulk sound speed increases at a faster rate at lower temperatures under high pressure but increases linearly with decreasing temperature, otherwise.

The bulk sound speed contours in Figure 19 follow very similar patterns as the density contours for each of the ice shell boundary pressure cases. While the bulk sound speed decreases linearly with increasing temperature for both cases, it stays constant with changing pressure for the boundary pressure of 3.6 MPa and increases slowly with increasing pressures for the boundary pressure of 36.15 MPa. The higher boundary pressure case for the bulk sound speed experiences a sharper change in color than that of the density contour plot, even though they look very similar at first glance. The similarity in the bulk sound speed and density plots follows what we would expect: the speed of sound depends on both the bulk modulus and the density of the material, and thus, if the density changes by a certain amount, so should the speed of sound through that material.

3.1.2 Ice Shell Models

To understand the most fundamental thermodynamic and seismic properties of the Europan ice shell, we take a closer look at density and the seismic wave velocities. Figure 20 shows the density of Ice Ih for (top left) a depth of 3 km and surface temperature of 50 K, (top right) a depth of 3 km and surface temperature of 140 K, (bottom left) a depth of 30 km and surface temperature

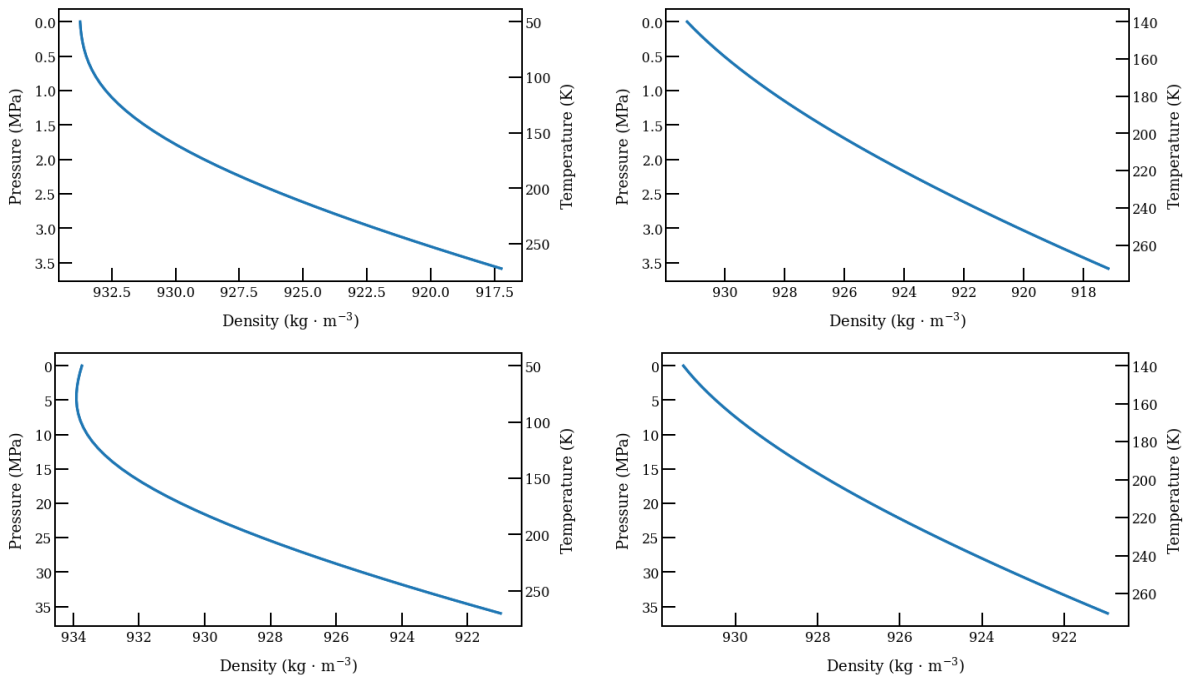

Figure 20: Density for Ice Ih as a function of depth using pressure and temperature conditions comparable to the Europan ice shell. **Top:** Depth of 3 km with an ice-ocean boundary pressure of 3.6 MPa with surface temperatures of (left) 50 K and (right) 140 K. **Bottom:** Depth of 30 km with an ice-ocean boundary pressure of 36.15 MPa with surface temperatures of (left) 50 K and (right) 140 K. While the models are all relatively linear, there exists an inversion with the density near the surface for the low surface temperature cases (top and bottom left) that is more intense with the deeper model (bottom left).

of 50 K, and (bottom right) a depth of 30 km and surface temperature of 140 K. The same order of appearance of pressure-temperature conditions for the four plots in Figure 20 is followed by the four plots in both Figures 21 and 22, where they show the resulting p-wave velocities and s-wave velocities, respectively.

Figure 20 gives the density profile for the ideal ice shell on Europa from the surface down to the ice-water boundary. Overall, the density shows a relatively linear trend with respect to depth, except at colder surface temperatures. The two plots on the left side of Figure 20 show the density experiencing a curve near temperatures between 50 K and 100 K. The bottom left plot even shows an inversion curve, where the density increases slightly at depths just below the surface before it switches to decrease. This point occurs around a depth where the pressure is 5 MPa and

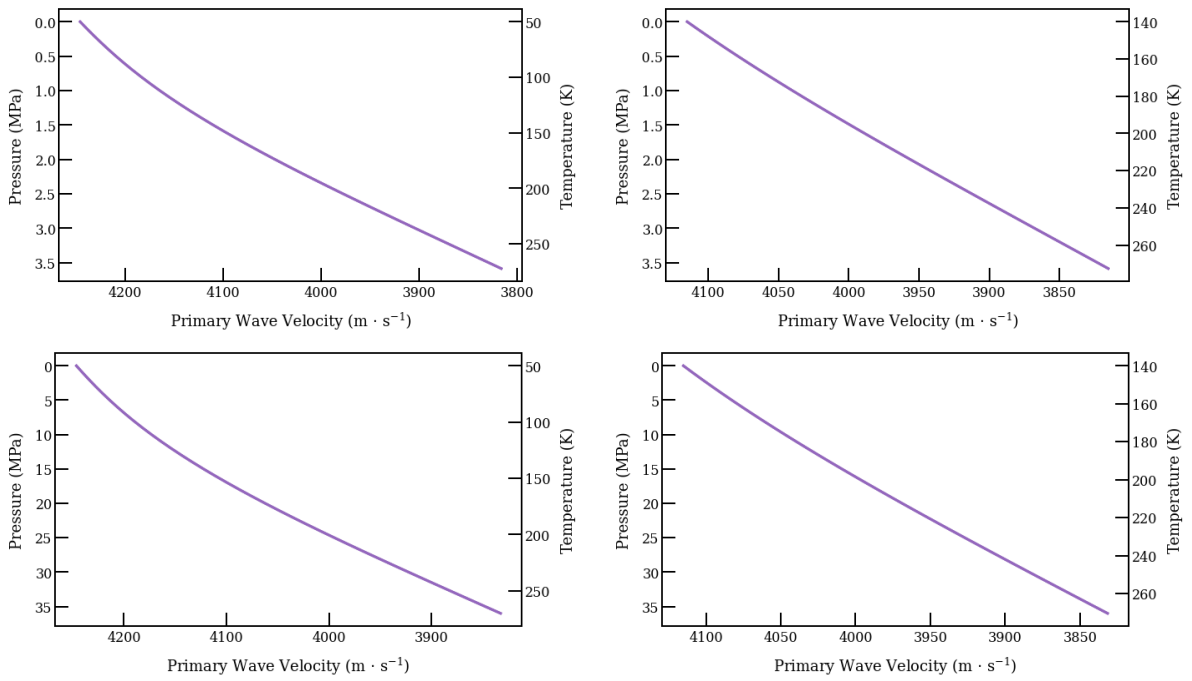

Figure 21: P-wave velocity for Ice Ih as a function of depth using pressure and temperature conditions comparable to the Europan ice shell. **Top:** Depth of 3 km with an ice-ocean boundary pressure of 3.6 MPa with surface temperatures of (left) 50 K and (right) 140 K. **Bottom:** Depth of 30 km with an ice-ocean boundary pressure of 36.15 MPa with surface temperatures of (left) 50 K and (right) 140 K. The models all show relatively linear relationships, with a slight bend in both of the low surface temperature cases (top and bottom left).

the temperature is approximately 70 K. The two plots on the right side of Figure 20 use higher surface temperatures and are much more linear than the other two plots. However, the higher-surface temperature density lines both show a slight curve starting close to the middle depth and continuing up to the surface.

Figure 21 gives the p-wave velocities as functions of depth for each of the four different surface temperature-depth combinations (given in the same order as the density plots). All of the p-wave velocity graphs show a distinct linear trend, but each have varying amounts of curvature that resemble the two right side plots of the density in Figure 20. The two plots on the left side show more pronounced curves than the ones on the right, where the ones on the right are extremely linear.

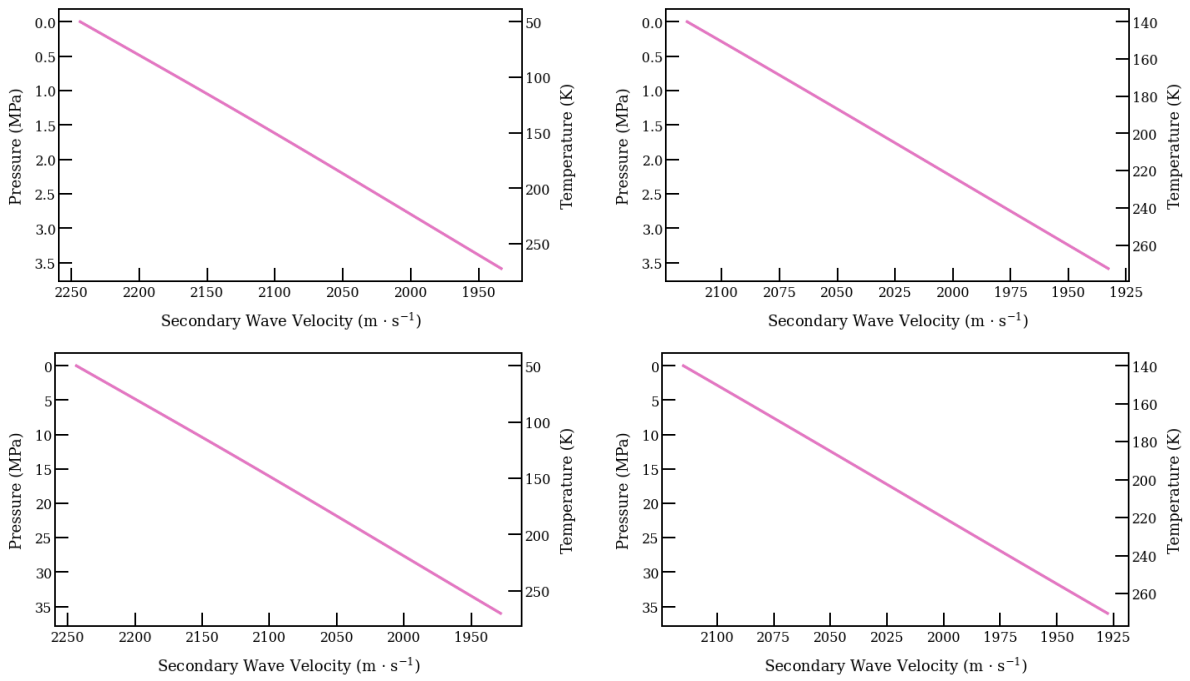

Figure 22: S-wave velocity for Ice Ih as a function of depth using pressure and temperature conditions comparable to the Europan ice shell. **Top:** Depth of 3 km with an ice-ocean boundary pressure of 3.6 MPa with surface temperatures of (left) 50 K and (right) 140 K. **Bottom:** Depth of 30 km with an ice-ocean boundary pressure of 36.15 MPa with surface temperatures of (left) 50 K and (right) 140 K. The models all show relatively linear relationships.

The s-wave velocities as functions of depth are shown in Figure 22, and they all seem to be extremely linear, as well. The difference with the seismic velocities shown in Figure 22, as opposed to the right side of Figure 21, is that all of the lines are only very slightly curved in a concave-down pattern, while those for p-wave velocity are curved in a concave-up pattern.

3.2 Salt-Water Experiments

The raw data of the saltwater freezing point analysis experiments are measurements of resistance over time, which we convert to temperature using Equation 6,

$$T = 2.553R - 255.29 \tag{6}$$

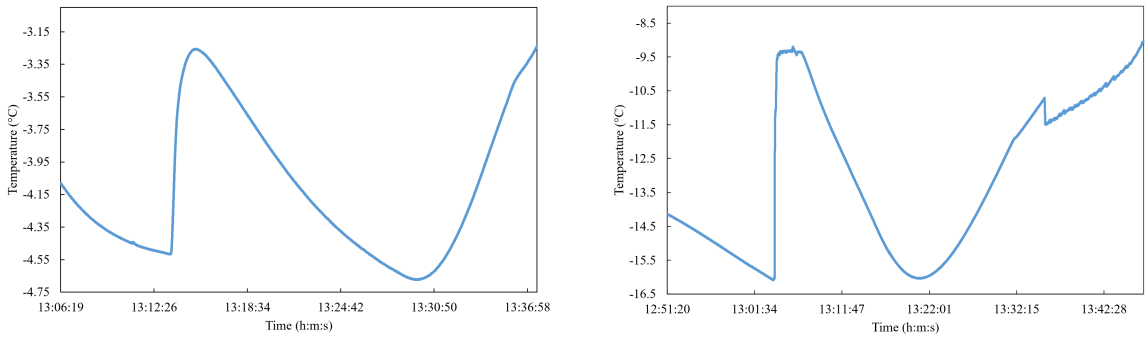

Figure 23: *Varying Pressure.* Two freezing curves of saltwater, which show the temperature of the sample in Celsius as a function of the time of day the experiment was performed in hours, minutes, and seconds. **Left:** The NaCl 5% concentration sample under a constant pressure of 0.00 MPa $\pm$ 1.72 MPa. This trial was done on October 22, 2020. The freezing point for this sample is evaluated to be -3.26 °C $\pm$ 0.16 °C. **Right:** The NaCl 5% concentration sample under a constant pressure of 68.95 MPa $\pm$ 1.72 MPa. This trial was done on October 11, 2019. The freezing point for this sample is evaluated to be -9.50 °C $\pm$ 0.20 °C.

where T is the temperature in Celsius and R is the resistance in Ohms (Ω). Equation 6 was derived from the conversion rates between resistance and temperature provided by the manufacturer of the RTD sensor, Omega Engineering, Inc. We analyze each experimental run's data one at a time, where we first convert the resistance measurements to temperature, and then plot the temperature over time. This gives us a freezing curve of temperature as a function of time that is shown as an example in Figure 13 in Section 2.2, and is shown in Figures 23 and 24. We determine the freezing point temperature for each trial by finding the maximum value of the peak or plateau of its freezing curve. We know the plateau temperature value to be the freezing point because it is where all of the energy in the system is focused on making the phase change occur within the entire sample. Once the sample is completely frozen, it begins to cool down again and find equilibrium with the temperature of the surrounding anti-freeze bath.

Figure 23 compares the freezing curves for one low pressure case of 0.00 MPa $\pm$ 1.72 MPa and one high pressure case of 68.95 MPa $\pm$ 1.72 MPa for the 5% NaCl sample. The most notable difference between these freezing curves is the plateau value, where the low pressure case has a value of -3.26 °C $\pm$ 0.16 °C and the high pressure case has a value of -9.50 °C $\pm$ 0.20 °C. Another difference is the shape of the curve, where the high pressure case has a more distinct plateau

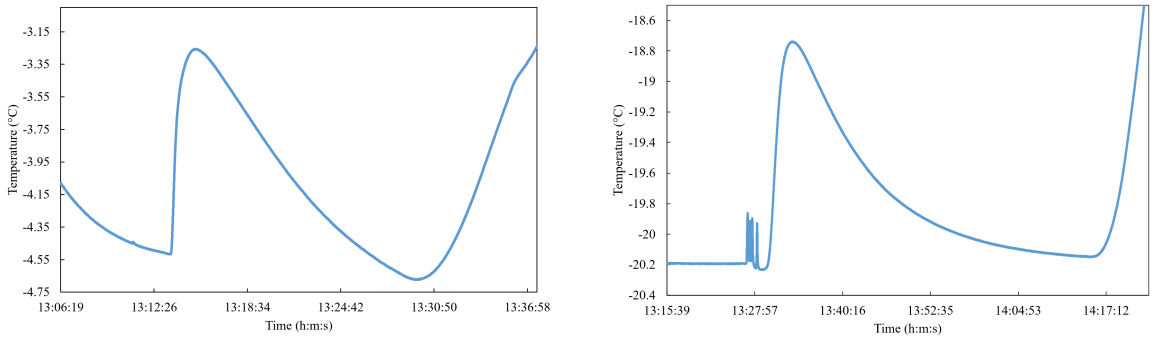

Figure 24: *Varying Salinity.* Two freezing curves of saltwater, which show the temperature of the sample in Celsius as a function of the time of day the experiment was performed in hours, minutes, and seconds. **Left:** The NaCl 5% concentration sample under a constant pressure of 0.00 MPa $\pm$ 1.72 MPa. This trial was done on October 22, 2020. The freezing point for this sample is evaluated to be -3.26 °C $\pm$ 0.16 °C. **Right:** NaCl 20% concentration sample under a constant pressure of 0.00 MPa $\pm$ 1.72 MPa. This trial was done on October 15, 2021. The freezing point for this sample is evaluated to be -18.75 °C $\pm$ 0.26 °C.

feature, while the low pressure case looks more rounded at its peak. The temperatures right before the base of the peak on both curves show the temperature decreasing before suddenly increasing into the plateau. This shows that during the process of undercooling, the sample spontaneously froze due to the low temperature environment. The tails at the end of the curves are from when the sample was brought back to room temperature after the full peak had been recorded. The small change in temperature within the tail in the high pressure case was caused by a shift in the pressure screw-pump to relieve some of the pressure out of the system while it was warming back up. The time between when the sample starts to release latent heat and when it has cooled back to its original temperature is the same for both the low and high pressure cases of the 5% NaCl sample. It took about 20 minutes for both samples to complete this section of the curve.

Figure 24 compares the freezing curves between low and high salinity at constant pressure (0.00 $\pm$ 1.72 MPa), where the left plot is the 5% NaCl solution and the right plot is the 20% NaCl solution. The low salinity case is the same as the low pressure case in Figure 23, and, as mentioned before, it has a plateau value of -3.26 °C $\pm$ 0.16 °C. The high salinity case has a much lower plateau value of -18.75 °C $\pm$ 0.26 °C. Both of the curves show a more rounded peak at their plateaus, as

opposed to the very flat plateau feature on the high pressure case in Figure 23. The time it takes from when the samples initially release latent heat to when they return to their original temperature differs between the varying salinity samples. The 5% NaCl sample takes 20 minutes to complete this process, while it takes the 20% NaCl sample approximately 37 minutes. This is most likely because the higher salinity sample needs to be in much colder temperatures in order to freeze. It can also be because of the difference in distance between the base and plateau temperature for the different samples. The lower salinity sample begins its latent heat release at a temperature of about -4.50 °C ± 0.20 °C and plateaus at -3.26 °C ± 0.16 °C, which is a difference of about 1.24 °C. Meanwhile, the higher salinity sample begins its latent heat release at a temperature of about -20.2 °C ± 0.20 °C and plateaus at -18.75 °C ± 0.26 °C. The higher salinity sample thus has a temperature difference from the base to the peak of about 1.45 °C, which is very close to that of the lower salinity sample. This means that it must take longer to return to its original temperature based mostly on the system's inherent cooling rate. Throughout the experiments, the freezing tank and pressure vessel both take much longer to reach very cold temperatures, such as those approaching -20 °C or lower, as opposed to warmer ones, such as -3 °C or even -10 °C. A more notable difference between the two salinity cases is the initial triggering of the freezing process: the lower salt concentration sample began freezing solely from the cold temperatures introduced with undercooling. The higher salt concentration sample needed more of a push, where we triggered the freezing process by rapidly increasing and decreasing the pressure, as if we were poking the sample itself. This sharp change in pressure is visible as a grouping of spikes at the base of the 20% NaCl sample freezing curve. This process of rapidly changing the pressure to make the sample begin freezing is not the most ideal for keeping our experiments as controlled as possible. Thus, there is ongoing work in developing a better technique to trigger this process, which is explained in Section 4.1.

Table 4 gives the full results of the saltwater experiments. The first column gives each of the salt solution concentrations, followed by the second column with each constant pressure value that we analyzed. We used the same five pressure values (0.00 MPa, 17.24 MPa, 37.47 MPa, 51.71

Concentration	Pressure (MPa) ± 1.72 MPa	# of Freezing Measurements	Average Freezing Point (°C)	Standard Deviation Uncertainty (°C)
NaCl 5%	0.00	16	-3.40	± 0.16
	17.24	12	-4.77	± 0.13
	34.47	9	-6.09	± 0.15
	51.71	6	-7.79	± 0.13
	68.95	1	-9.50	± 0.20
NaCl 10%	0.00	9	-7.44	± 0.16
	17.24	5	-8.68	± 0.32
	34.47	3	-10.24	± 0.16
	51.71	3	-11.44	± 0.07
	68.95	4	-13.36	± 0.13
NaCl 20%	0.00	5	-18.64	± 0.26
	17.24	4	-20.85	± 0.67
	34.47	2	-21.39	± 0.24
	51.71	2	-23.17	± 0.08
	68.95	1	-25.07	± 0.20

Table 4: Freezing point experiment results. From left to right, the table gives the by-weight percentage concentration of the NaCl sample, the constant pressure used for each set of trials (given in MPa) with associated uncertainty of ± 1.72 MPa, the number of successful trials that yielded analyzable freezing point temperatures, the average freezing point temperature across trials for each constant pressure setting (given in Celsius), and the associated uncertainty for the average freezing point temperatures (given in Celsius), which was found by calculating the standard deviation.

MPa, and 68.95 MPa, all with an uncertainty of ± 1.72 MPa) within each of the three NaCl-water solution analyses. The third column gives the total number of freezing measurements taken per constant pressure value within each sample group. We performed numerous trials for each of the saltwater experiments and yielded a total of 82 successful trials where the sample froze. The fourth column gives the average freezing point temperature for the group of experiments done under each constant pressure value. These numbers are based on the number of freezing temperature measurements gathered per constant pressure group, where some use more than ten measurements, while others use less than five or only one. The uncertainty associated with the average freezing point temperatures is given in the fifth and final column, which were determined through standard deviation of the freezing temperature measurements used in the average. For the points that only had one freezing point measurement, we use the average value of the rest of the uncertainties for the entire set of data, which is ± 0.20 °C. An important aspect that Table 4 shows is that

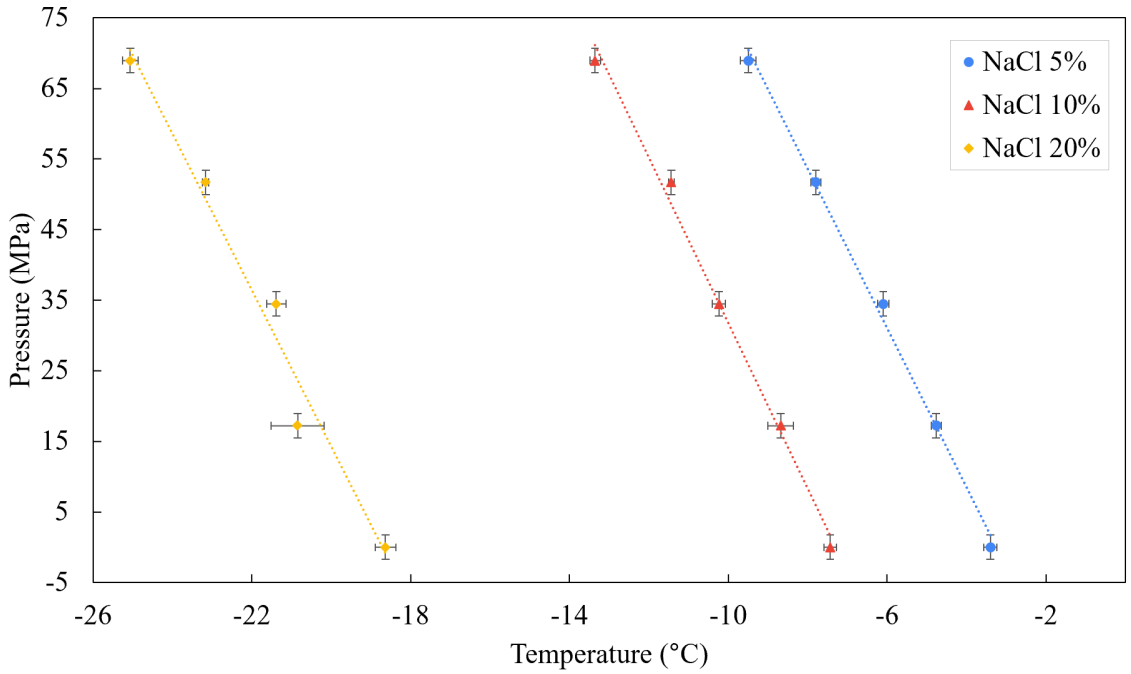

Figure 25: The average freezing point temperatures (given in Celsius) for each NaCl sample as a function of pressure (given in MPa). The blue circles denote the 5% NaCl concentration, the red triangles denote the 10% NaCl concentration, and the yellow diamonds denote the 20% NaCl concentration. Error bars are shown as the uncertainties in the freezing point temperatures and associated pressures. The slopes for the 5%, 10%, and 20% samples' trend lines are (-11.28 $\pm$ 0.34) MPa $^{\circ}C^{-1}$, (-11.73 $\pm$ 0.53) MPa $^{\circ}C^{-1}$, and (-11.08 $\pm$ 1.01) MPa $^{\circ}C^{-1}$, respectively.

our results are reproducible. For example, we took 16 measurements of the 5% NaCl solution under approximately 0 MPa of constant pressure which resulted with an average freezing point uncertainty of 0.16 °C, which is a very accurate measurement of temperature when compared to previous studies.

Figure 25 plots the average freezing point temperatures from Table 4 for each sample across all constant pressure values with associated uncertainty given by the error bars. The uncertainty in the pressure values is approximately $\pm$ 1.72 MPa, which is the error value determined from the readings on the pressure screw-pump system gauge. All of the samples, the 5%, 10%, and 20% NaCl concentrations, show distinct linear trends with slope values of (-11.28 $\pm$ 0.34) MPa $^{\circ}C^{-1}$, (-11.73 $\pm$ 0.53) MPa $^{\circ}C^{-1}$, and (-11.08 $\pm$ 1.01) MPa $^{\circ}C^{-1}$, respectively. The slopes and slope uncertainties were determined using linear regression. The slopes for each line are all equivalent

within uncertainty, and their equivalence shows there is a very consistent linear trend between pressure and freezing point temperature for all different salinity samples, given that their salinity is constant when adjusting the pressure. Additionally, as we increase the salt concentration, the freezing point temperature also decreases somewhat linearly. Thus, as we increase both the pressure and the concentration, the freezing point temperature decreases much faster than if we increase only one of the variables. Moreover, the addition of salt and increase in pressure combined allowed us to obtain a freezing point depression of over -20 °C at our most extreme conditions compared to pure water at 0 MPa.

4 Discussion

The computational results given by the models of Europa's ice shell shown in Sections 3.1.1 and 3.1.2 make many assumptions that are important to take into account when analyzing them. The first is that the ice shell changes in temperature linearly with depth. If the actual Europan ice shell has a nonlinear temperature gradient with respect to depth, which is probable given the possibility of ice shell convection (Figure 2), then these models would not be directly applicable to the icy moon. Nevertheless, the linear temperature gradient provides us with an ideal starting point and thus is still important to investigate as the perfect-world case. The models also assume ice shell depth estimates of 3 km and 30 km which have been previously established by the literature as the possible boundaries to the ice shell thickness. An important thing to note is that the ice shell may not necessarily be 3 km or 30 km, and it could instead be some value in between. Our models, by using the two extremes for the depth, can be used to indirectly identify how the different properties of ice would change if the depth (h) was 3 km $< h <$ 30 km. Additionally, SeaFreeze assumes that the substance used in the computational analysis is pure water (H_2O) and its various ice types; this is because it has not yet been developed to analyze saltwater solutions. Moreover, our models assume that the ice shell is uniformly only pure-water ice, meaning we assume there are no extraneous particles, trapped rocks, air pockets, potential microorganisms, or other objects that are not strictly H_2O as the Ice Ih ice type. Given all of these assumptions, we ultimately assume a uniform, idealized ice shell of Ice Ih between thicknesses of 3 km and 30 km that changes temperature linearly with depth. We use this ideal case to understand its thermodynamic and seismic properties with respect to depth. We attempt to ground our models in reality by applying the results of our saltwater freezing experiments because Europa's ice layer is known to have some concentration of salts.

For our ice shell models, the only difference between the left and right sides of Figures 20-22 is that the left side begins with a colder surface temperature. Thus, the colder surface temperature seems to have a greater effect on the curvature of the density and seismic wave velocities

as functions of depth. These density and seismic wave velocity plots also all relatively follow what we would expect based on the results of the contour plots outlined in Figures 14-16 in Section 3.1.1. The density contours at high pressures show a more curved distribution, which is reflected in the depth-density curves. Similarly, the seismic wave velocities seem to have seemingly linear relationships with temperature in the contour plots, and this is reflected in both of their plots as linear functions of depth in Figures 21 and 22. While the models can explore the thermodynamics and seismic profiles within an ice shell similar to that on Europa, the saltwater experiments can help us constrain the physical properties of the actual ice shell.

Our experiments yielded extremely consistent results regarding how the freezing point temperature changes with varying salt concentration and pressure. We found that as the pressure increased and as the concentration level of NaCl increased, the freezing point temperature of the saltwater solution would decrease. We can apply these results to our pure-water ice shell models to understand what would happen if we could add NaCl. We would first find that the temperature found for the ice-water boundary (Section 2.1.1, Figure 6) would need to be at a much lower value for both the 3 km and 30 km ice shell thicknesses. This is because adding NaCl to pure water, as shown in our saltwater experiments, causes the freezing point temperature to decrease significantly; thus, the temperature needed at the ice-water boundary would be much lower than the one used for the pure water models. Since the ice-water boundary temperature would be much lower, we expect that the models for the ideal ice layer would be cut off at some lower temperature and therefore truncate the curves shown in Figures 20-22, assuming saltwater follows the same density and seismic wave profile as that of pure water. Regardless of adding saltwater to the ice shell models, the models still make many assumptions, which may or may not reflect the real conditions of Europa's ice shell. They provide an ideal case as a starting point for understanding the thermodynamics and seismic profile of the ice shell, while the saltwater experiments help us constrain the ice shell's physical properties and possibly its true thickness.

4.1 Future Work

We plan on continuing our investigation into Europa's hydrosphere both with the computational models and saltwater experiments. One of the next steps in modeling the hydrosphere includes analyzing the ocean layer using SeaFreeze to calculate the thermodynamic and seismic properties of pure liquid water. We would make similar assumptions as we did for the ice shell because of the current limits of SeaFreeze functionality. However, there is ongoing development occurring with the end goal of SeaFreeze being able to analyze the thermodynamic and seismic properties of different salt concentrations, which would allow us to make more accurate models with respect to Europa's actual conditions.

We also plan to continue the saltwater experiments by exploring the phase diagram of different magnesium sulfate ($MgSO_4$) and potassium chloride (KCl) solutions. Using the same methods as we did for the NaCl experiments, we will find the freezing point temperatures of 5%, 10%, and 20% $MgSO_4$ and KCl concentrations at varying pressures between 0 MPa and 70 MPa. Once we have collected the freezing temperature data for $MgSO_4$ and KCl, we will begin investigating the phase diagram of a solution that uses a combination of two or all three salts. Looking into the freezing point temperatures of solutions that use more than one type of salt might be the most relevant to Europa's hydropshere because it is unquestionably more complex than a solution containing only NaCl and water.

There are several plans that we are currently working on to make the experiments more precise and accurate. One such plan is remeasuring the salinity of the NaCl samples. The samples were initially made over a year ago, and we are interested in seeing whether the salinity may have slightly changed. There are also plans for making the freezing triggering process more streamlined, where we have installed a transducer inside the pressure vessel. Implementing the transducer as the catalyst to the freezing process will enable the pressure screw-pump system to solely be used for keeping the system pressure constant and for fine pressure adjustments. We are currently testing

the effectiveness of the transducer with the 5% $MgSO_4$ concentration at a constant pressure of 0 MPa. We are also currently taking calibration measurements of the RTD sensor, which will provide minor corrections to be applied to our freezing point measurements at a later date.

5 Conclusion

In this study, we explored the thermodynamic and seismic properties of Ice Ih under Europan-like conditions and conducted experiments to determine the dependence of the freezing point temperature of water on salinity and pressure. We found that for an ideal Europa-like ice shell, the density and seismic wave profiles tend to show very linear patterns, which is possibly due to the linear temperature gradient. However, there are some inversion effects with the density at shallower depths (i.e., at lower pressures) that also match the minor fluctuation within the p-wave velocity. We find very little changes within the s-wave velocity. In the thermodynamic property contour plots, the density and the bulk sound speed both experienced the largest effects with respect to pressure and temperature, which were visible only for higher pressures around 30 MPa. Finally, we find a very clear result with the saltwater experiments, which is that increasing the salinity of the solution, increasing the pressure, or increasing both simultaneously significantly decreases the freezing point temperature. At our most extreme conditions of 20% NaCl solution under almost 70 MPa of pressure, we obtain a freezing point temperature depression of more than 20 °C compared to pure water with no pressure. The decrease in freezing temperature between zero and high pressure is consistent for each saltwater sample. One of our most noteworthy accomplishments is finding the freezing point temperatures of these various solutions to higher precision than previous work, improving the temperature uncertainties by a full magnitude.

Our models, while useful for understanding the thermodynamics of Europa's ice shell, are very simple. We suggest that if we were to add NaCl to our ideal cases, they would experience a much lower ice-ocean boundary temperature than the ones predicted by our models. If the salt content in Europa's ice shell could be determined, then we would be able to use our results to predict the ice shell's thickness based on our saltwater freezing temperature results. Unfortunately, we only know some possible salts that may be present in the Europan hydrosphere, not the entire composition, which still allows us to make some constraints, even if we are not able to measure the true thickness.

Our investigation into the ice shell of Europa just scratches the surface of what we can discover about the icy ocean world. The Europa Clipper will be making its journey to the Jovian system in the late 2020s to uncover many of Europa's mysteries. Our study can help future studies in interpreting the Clipper's remote sensing data, especially our saltwater results, for which we plan to gather a full set of freezing temperatures across different salts at pressures relevant to Europa and the other icy moons. We look forward to expanding our knowledge of Europa and to possibly resolving the question surrounding its capability to host life.

Acknowledgements

This work was completed with support from the NASA Solar System Workings Grant number 80NSSC22K0136 as part of the "Phase Relations of Salt-H_2O Solutions at High Pressure: Implications for the Icy Worlds" project. Thank you to George Shaw, Co-Investigator, for his work on the experiment's high pressure system. Elise Liebow, Melanie Boyle, Srihari Balaji, and Manav Bilakhia at the Department of Physics and Astronomy of Union College (Schenectady, NY) helped in collecting the experimental data for this project. Revisions to this thesis were facilitated with the help from both Heather Watson, Principle Investigator, and Rebecca Koopmann. SeaFreeze was developed by Baptiste Journaux, J. Michael Brown, and Penny Espinoza at the Earth and Space department of the University of Washington (Seattle, WA). Finally, thank you to Heather Watson, for her support and guidance throughout the entire process for this thesis.

References

Brennan, P. (2020). Life in our Solar System? meet the neighbors – exoplanet exploration: Planets beyond our Solar System. *NASA's Exoplanet Exploration*.

Breuer, D., & Moore, W. B. (2015). Dynamics and thermal history of the terrestrial planets, the Moon, and Io. *Treatise on Geophysics: Second Edition*, *10*, 255–305.

Brown, J. M. (2018). Local basis function representations of thermodynamic surfaces: Water at high pressure and temperature as an example. *Fluid Phase Equilibria*, *463*, 18–31.

Collins, G., & Johnson, T. V. (2014). Ganymede and Callisto. *Encyclopedia of the Solar System*, 813–829.

Frank, M. R., Scott, H. P., Aarestad, E., & Prakapenka, V. B. (2016). Potassium chloride-bearing ice VII and ice planet dynamics. *Geochimica et Cosmochimica Acta*, *174*, 156–166.

Greenberg, R., Hoppa, G. V., Tufts, B. R., Geissler, P., Riley, J., & Kadel, S. (1999). Chaos on Europa. *Icarus*, *141*, 263–286.

Hoppa, G. V., Tufts, B. R., Greenberg, R., & Geissler, P. E. (1999). Formation of cycloidal features on Europa. *Science*, *285*, 1899–1902.

Hussmann, H., Sotin, C., & Lunine, J. I. (2015). Interiors and evolution of icy satellites. *Treatise on Geophysics: Second Edition*, *10*, 605–635.

Journaux, B., Brown, J. M., Pakhomova, A., Collings, I. E., Petitgirard, S., Espinoza, P., Ballaran, T. B., Vance, S. D., Ott, J., Cova, F., Garbarino, G., & Hanfland, M. (2020). Holistic approach for studying planetary hydrospheres: Gibbs representation of ices thermodynamics, elasticity, and the water phase diagram to 2,300 mpa. *Journal of Geophysical Research: Planets*, *125*.

Kane, S. R., & Gelino, D. M. (2012). The habitable zone and extreme planetary orbits. *Astrobiology*, *12*, 940–945.

Kleine, T., Münker, C., Mezger, K., & Palme, H. (2002). Rapid accretion and early core formation on asteroids and the terrestrial planets from Hf–W chronometry. *Nature 2002 418:6901*, *418*, 952–955.

Lowell, R. P., & DuBose, M. (2005). Hydrothermal sytems on Europa. *Geophysical Research Letters*, *32*, 1–4.

McKinnon, W. B. (2015). Effect of Enceladus's rapid synchronous spin on interpretation of Cassini gravity. *Geophysical Research Letters*, *42*, 2137–2143.

Moore, W. B., & Hussmann, H. (2009). Thermal evolution of Europa's silicate interior (R. T. Pappalardo, W. B. McKinnon, & K. K. Khurana, Eds.). *Europa (The University of Arizona Space Science Series)*, 369.

NASA, & JPL-Caltech. (2016). Artist rendering of Europa mission spacecraft. *NASA/JPL-Caltech*.

NASA, JPL-Caltech, & SETI-Institute. (2014). Pia19048: Europa's stunning surface. *NASA/JPL-Caltech*.

Pappalardo, R., Becker, T., Blaney, D., Blankenship, D., Burch, J., Christensen, P., Craft, K., Daubar, I., Gudipati, M., Hayes, A., Howell, S., Kempf, S., Kivelson, M., Klima, R., Korth, H., Mazarico, E., Paczkowski, B., Phillips, C., Rathbun, J., … Westlake, J. (2021). The Europa Clipper Mission: understanding icy world habitability and blazing a path for future exploration. *Bulletin of the AAS*, *53*.

Ronnet, T., Mousis, O., & Vernazza, P. (2017). Pebble accretion at the origin of water in Europa. *The Astrophysical Journal*, *845*, 92.

Schmidt, B. E., Blankenship, D. D., Patterson, G. W., & Schenk, P. M. (2011). Active formation of 'chaos terrain' over shallow subsurface water on Europa. *Nature 2011 479:7374*, *479*, 502–505.

Schubert, G., Anderson, J. D., Travis, B. J., & Palguta, J. (2007). Enceladus: Present internal structure and differentiation by early and long-term radiogenic heating. *Icarus*, *188*, 345–355.

Soderlund, K. M., Kalousová, K., Buffo, J. J., Glein, C. R., Goodman, J. C., Mitri, G., Patterson, G. W., Postberg, F., Rovira-Navarro, M., Rückriemen, T., Saur, J., Schmidt, B. E., Sotin, C., Spohn, T., Tobie, G., Hoolst, T. V., Vance, S. D., & Vermeersen, B. (2020). Ice-ocean exchange processes in the Jovian and Saturnian satellites. *Space Science Reviews*, *216*, 1–57.

Thomson, R. E., & Delaney, J. R. (2001). Evidence for a weakly stratified Europan ocean sustained by seafloor heat flux. *Journal of Geophysical Research: Planets*, *106*, 12355–12365.

Vance, S. D., Journaux, B., Hesse, M., & Steinbrügge, G. (2021). The salty secrets of icy ocean worlds. *Journal of Geophysical Research: Planets*, *126*, e2020JE006736.

Vreugdenhil, C. A., & Gayen, B. (2021). Ocean convection. *Fluids 2021, Vol. 6, Page 360*, *6*, 360.

Yeomans, D. K. (2006). Planetary satellite physical parameters. *JPL Solar System Dynamics*.

Appendices

Here we display the results from calculating various thermodynamic properties using SeaFreeze for different ice phases and across ice boundaries. We use the temperature and pressure values given in Table 2 as the boundary conditions for each of the ices.

Appendix A Properties Across Ices

In this section, we show results for density, Gibbs free energy, bulk sound speed, shear modulus, p-wave velocity, and s-wave velocity for Ice Ih, Ice II, Ice III, Ice V, and Ice VI phases.

Ice Ih

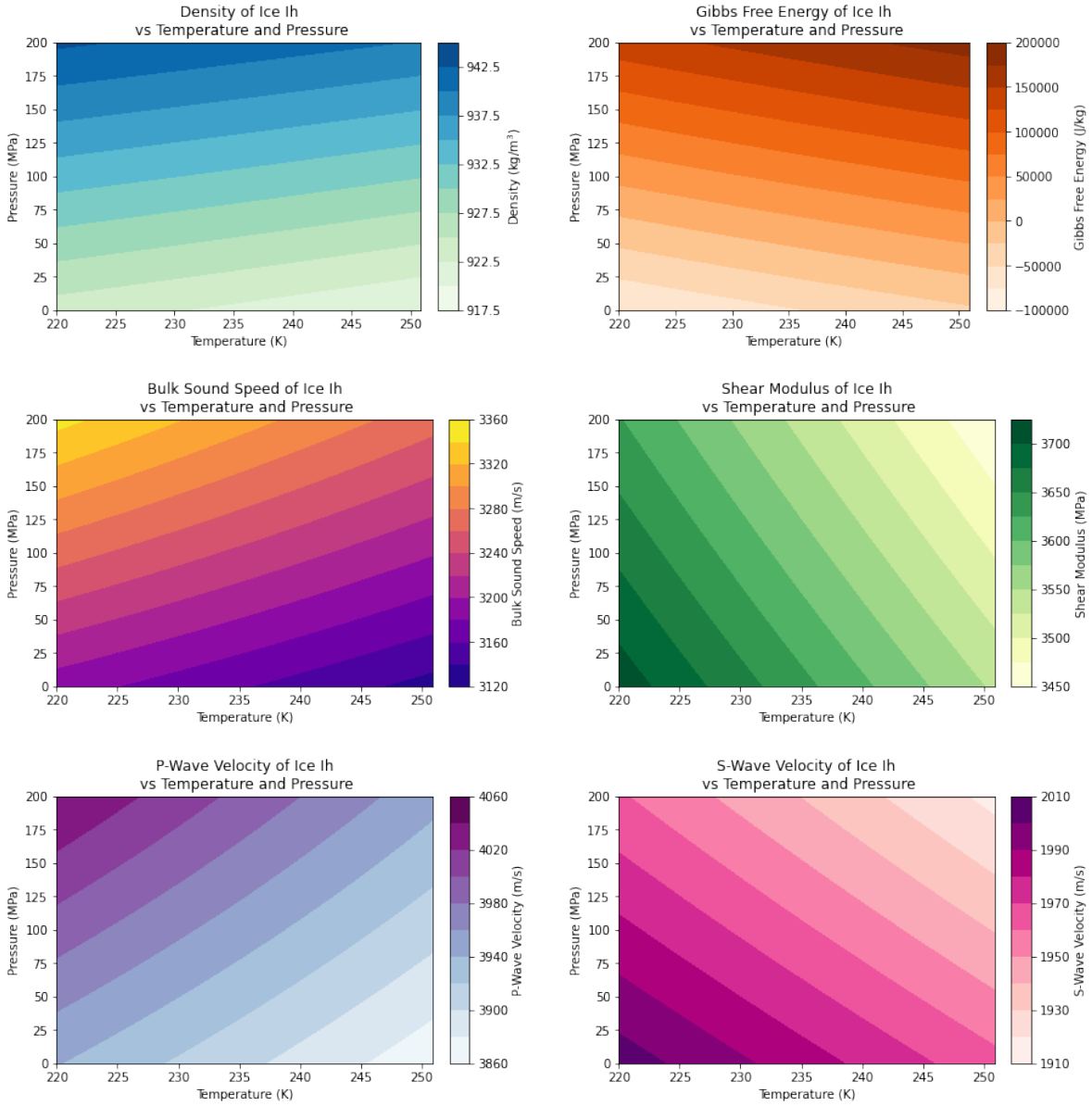

Figure 26: Thermodynamic properties for Ice Ih plotted as functions of temperature and pressure.

Ice II

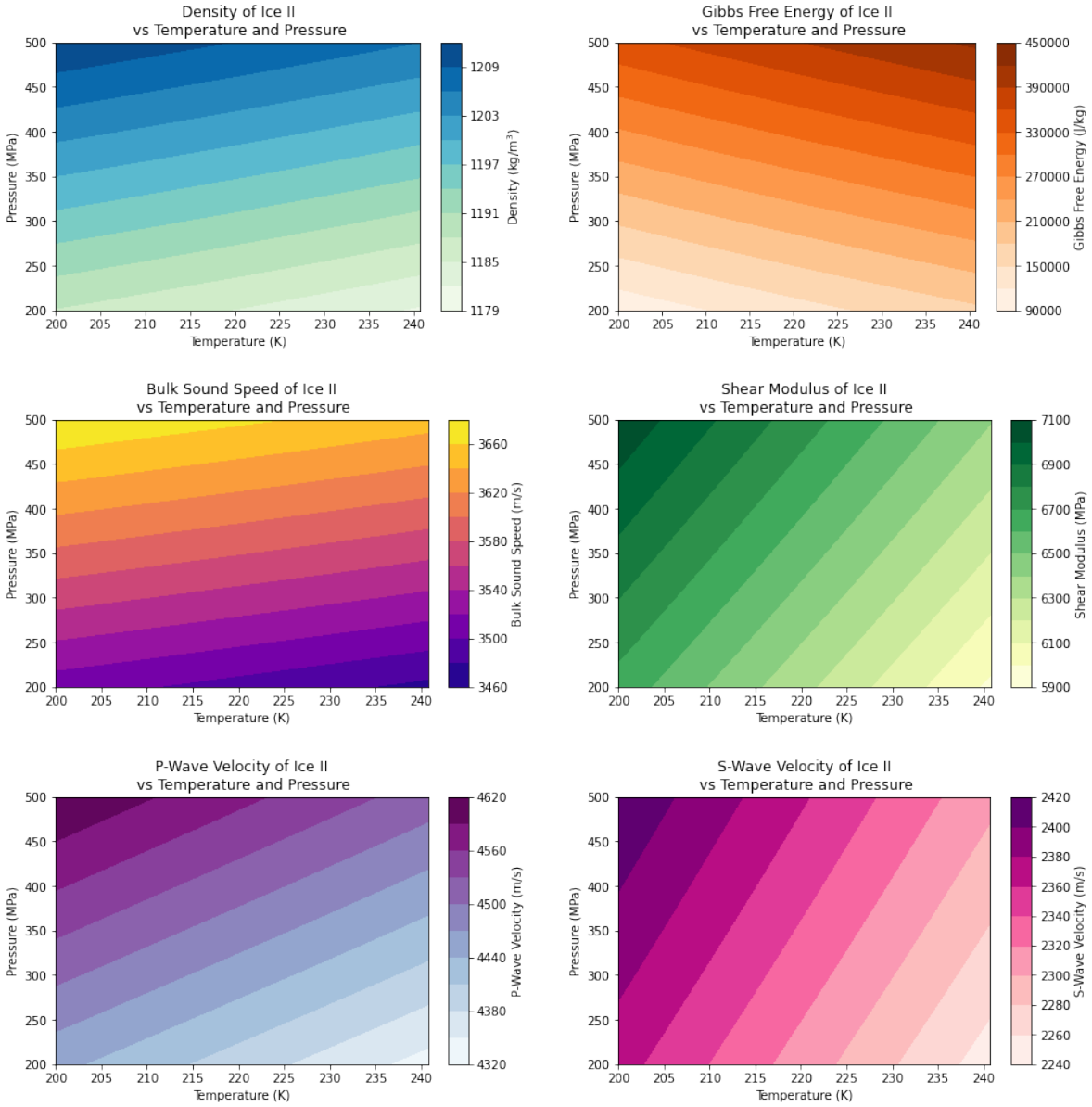

Figure 27: Thermodynamic properties for Ice II plotted as functions of temperature and pressure.

Ice III

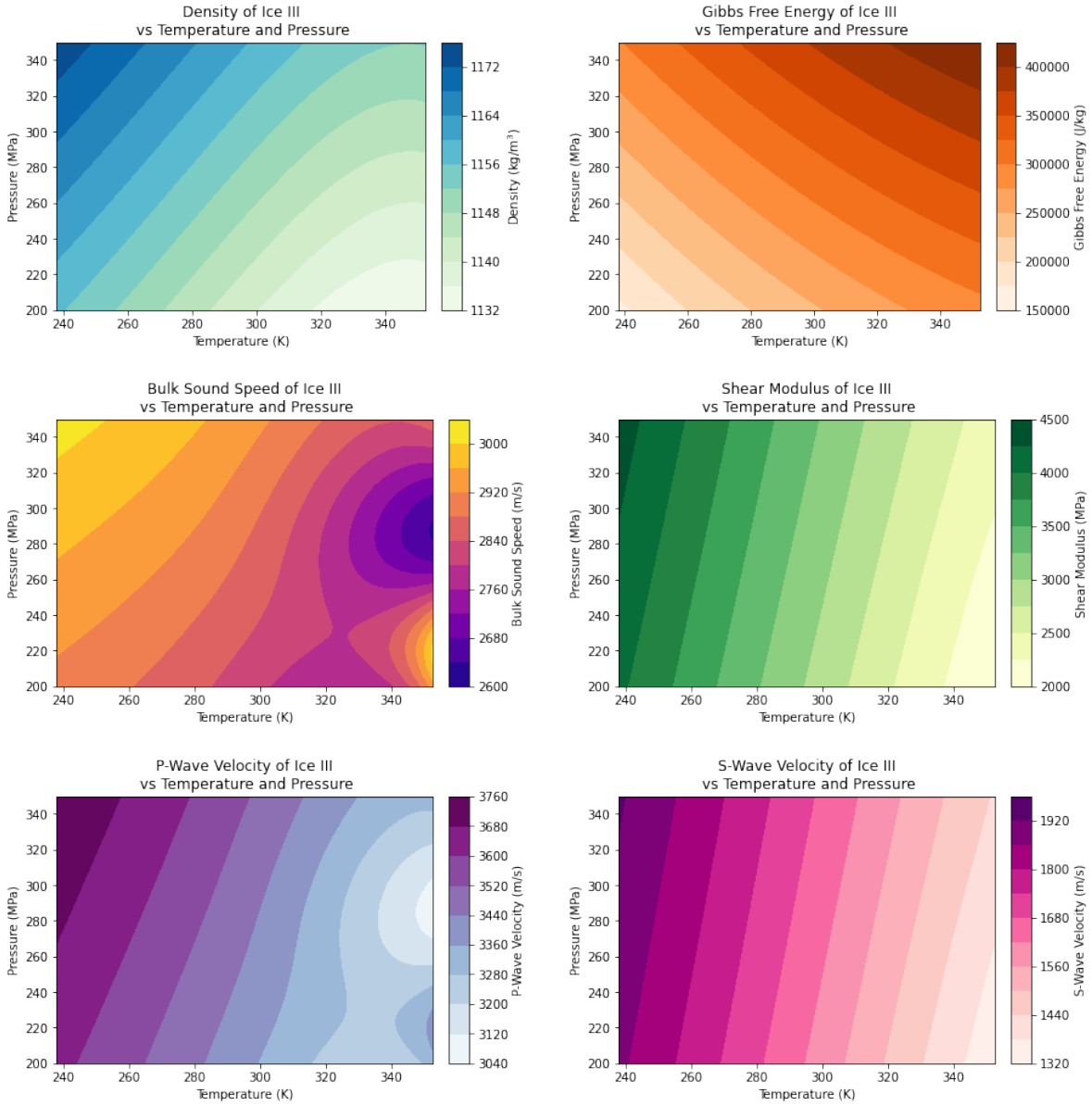

Figure 28: Thermodynamic properties for Ice III plotted as functions of temperature and pressure.

Ice V

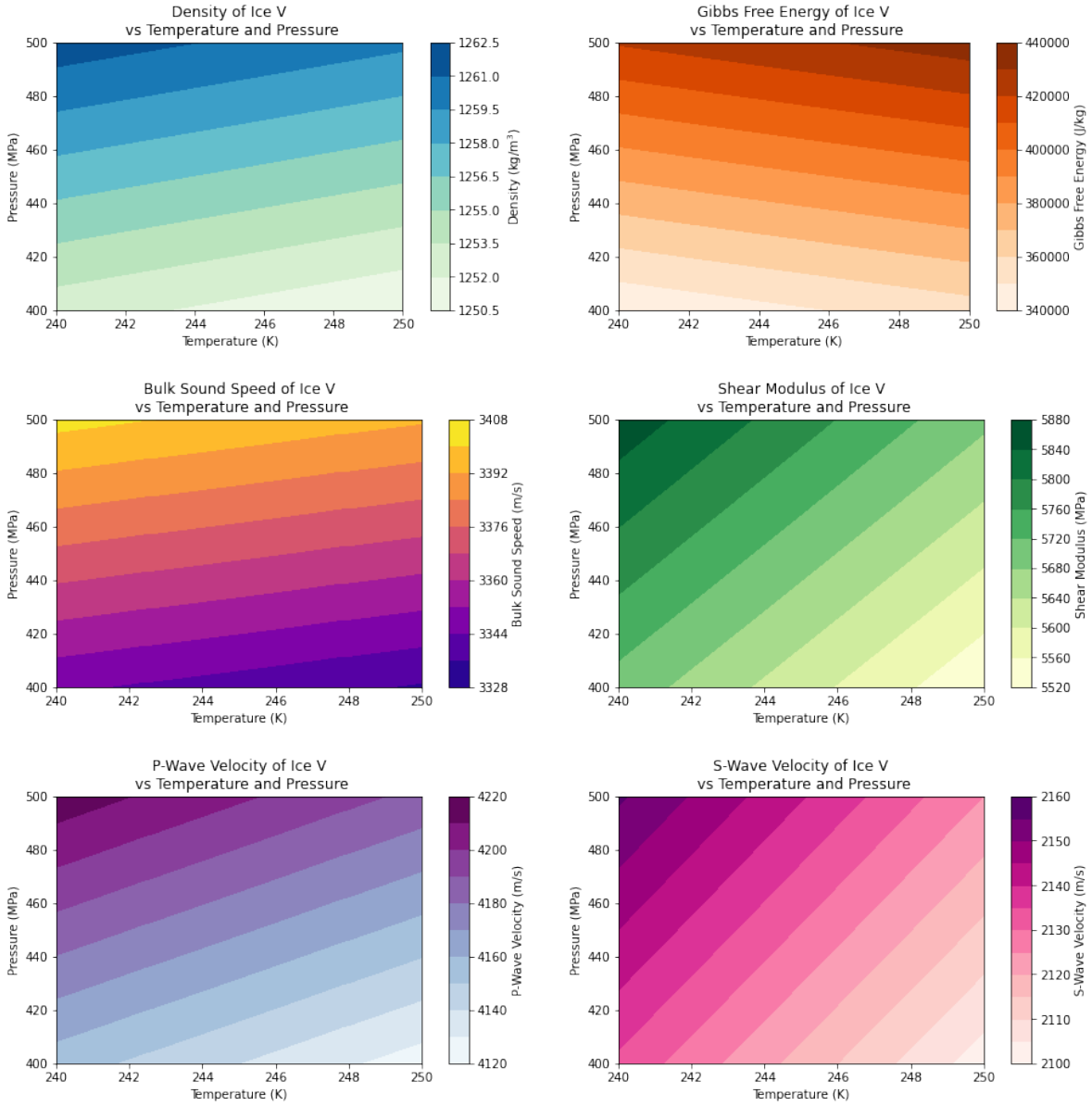

Figure 29: Thermodynamic properties for Ice V plotted as functions of temperature and pressure.

Ice VI

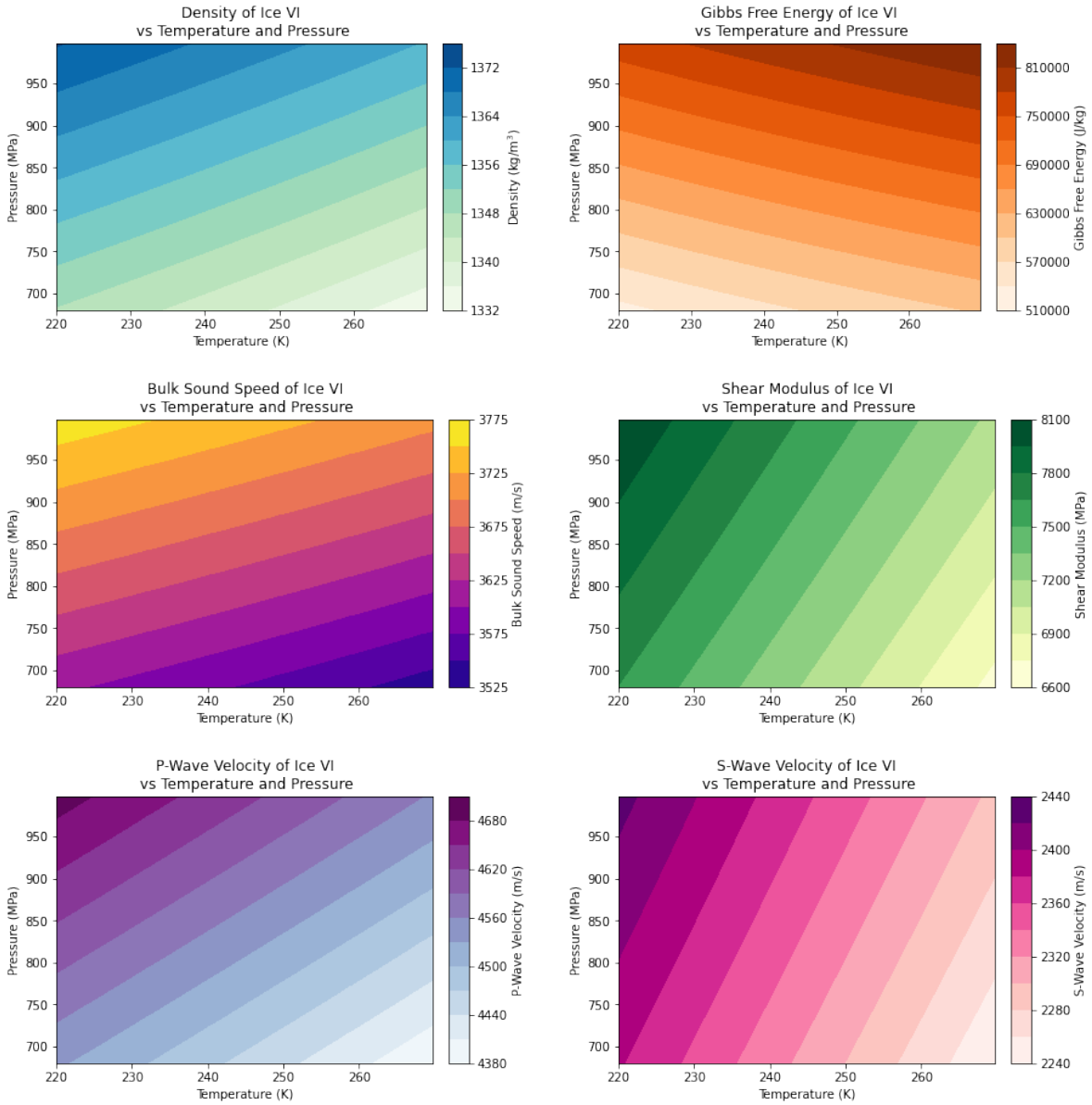

Figure 30: Thermodynamic properties for Ice VI plotted as functions of temperature and pressure.

Appendix B Properties Across Phase Boundaries

In this section, we show results for density, Gibbs free energy, bulk sound speed, shear modulus, p-wave velocity, and s-wave velocity across Ice Ih-Ice II, Ice Ih-Ice III, and Ice Ih-Ice III-Ice V

phase boundaries.

Ih-II Phase Boundary

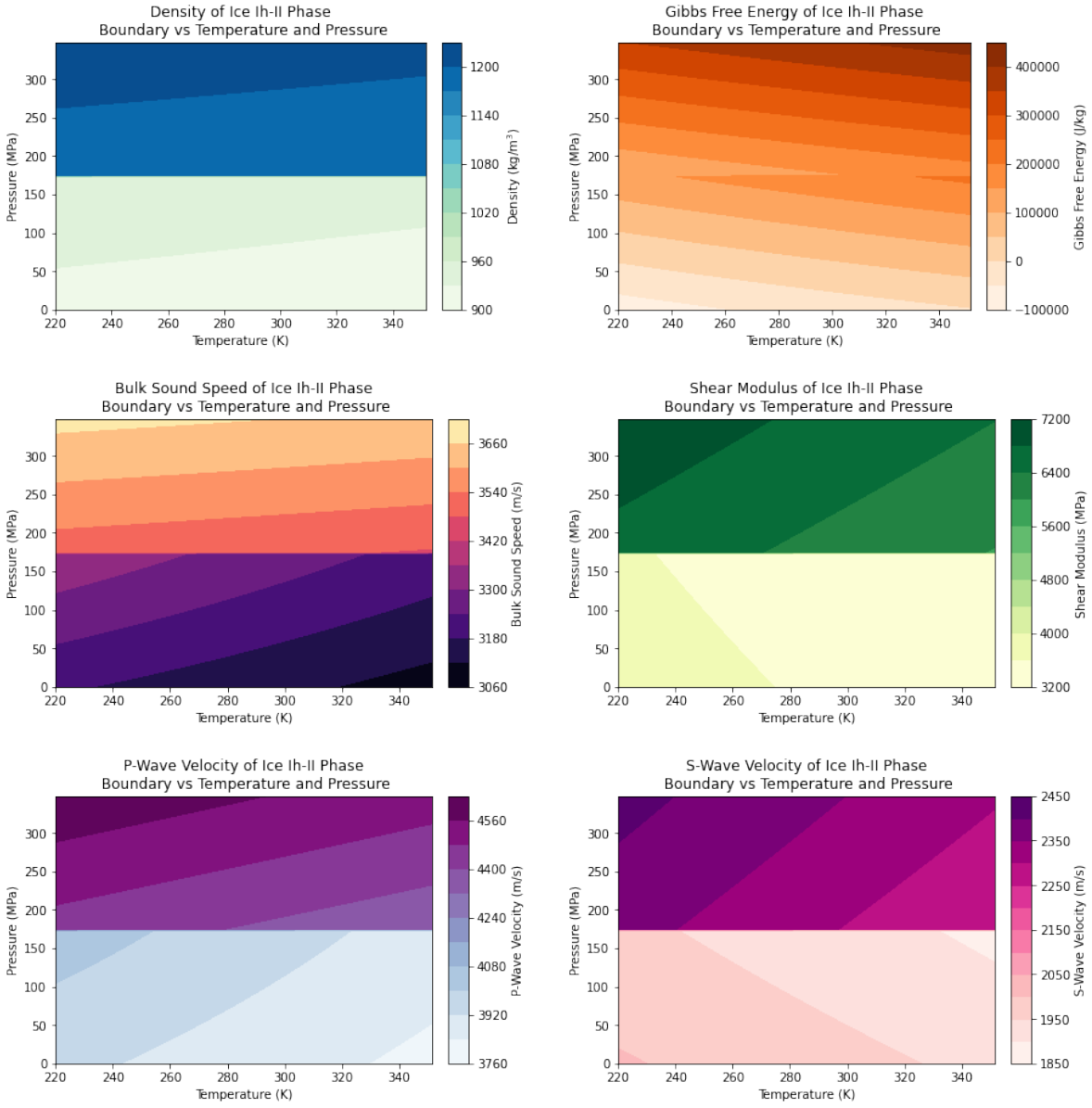

Figure 31: Thermodynamic properties for the solid-solid Ice Ih-Ice II phase boundary plotted as functions of temperature and pressure.

Ih-III Phase Boundary

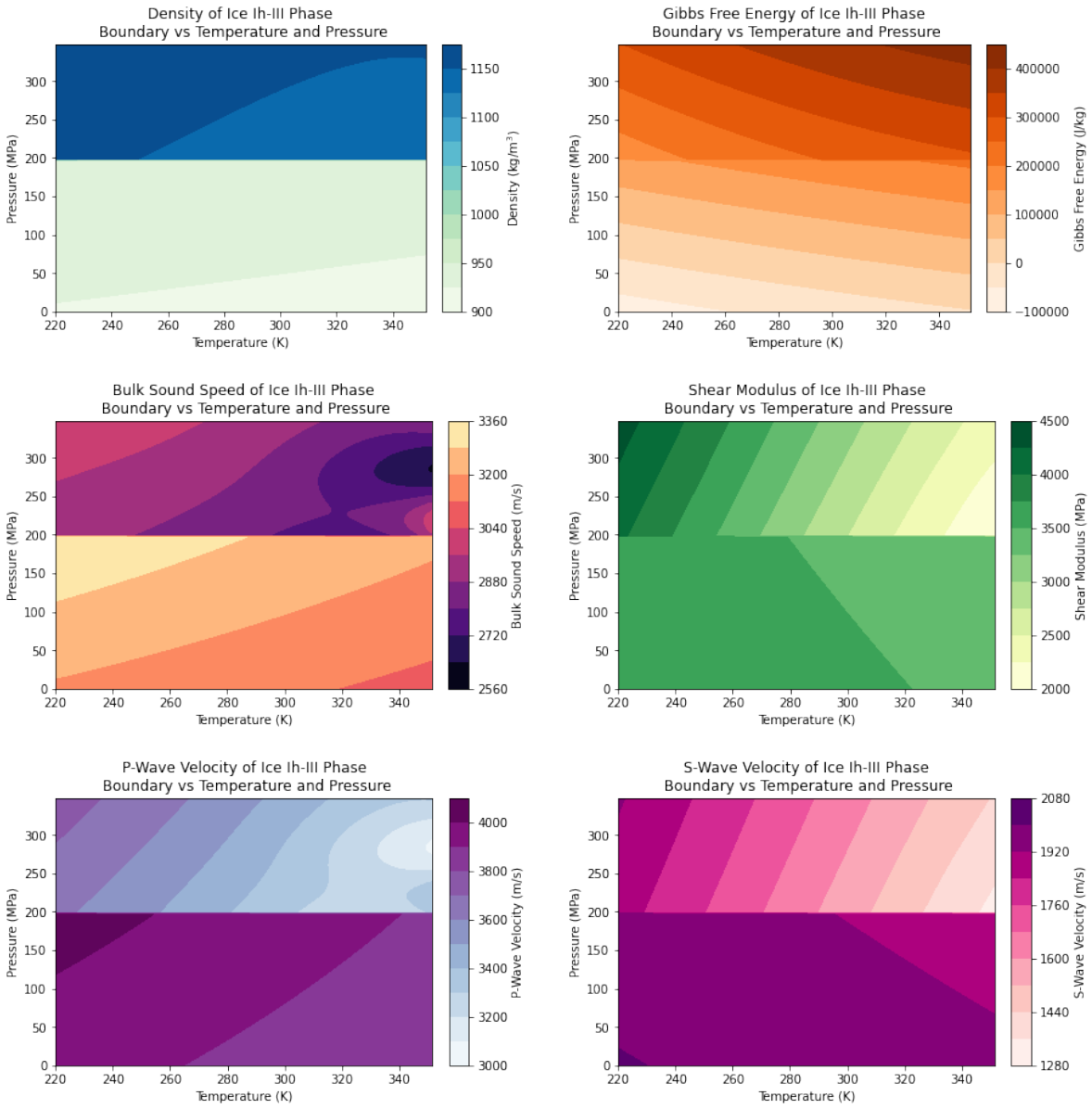

Figure 32: Thermodynamic properties for the solid-solid Ice Ih-Ice III phase boundary plotted as functions of temperature and pressure.

Ice Ih-Ice III-Ice V Phase Boundaries

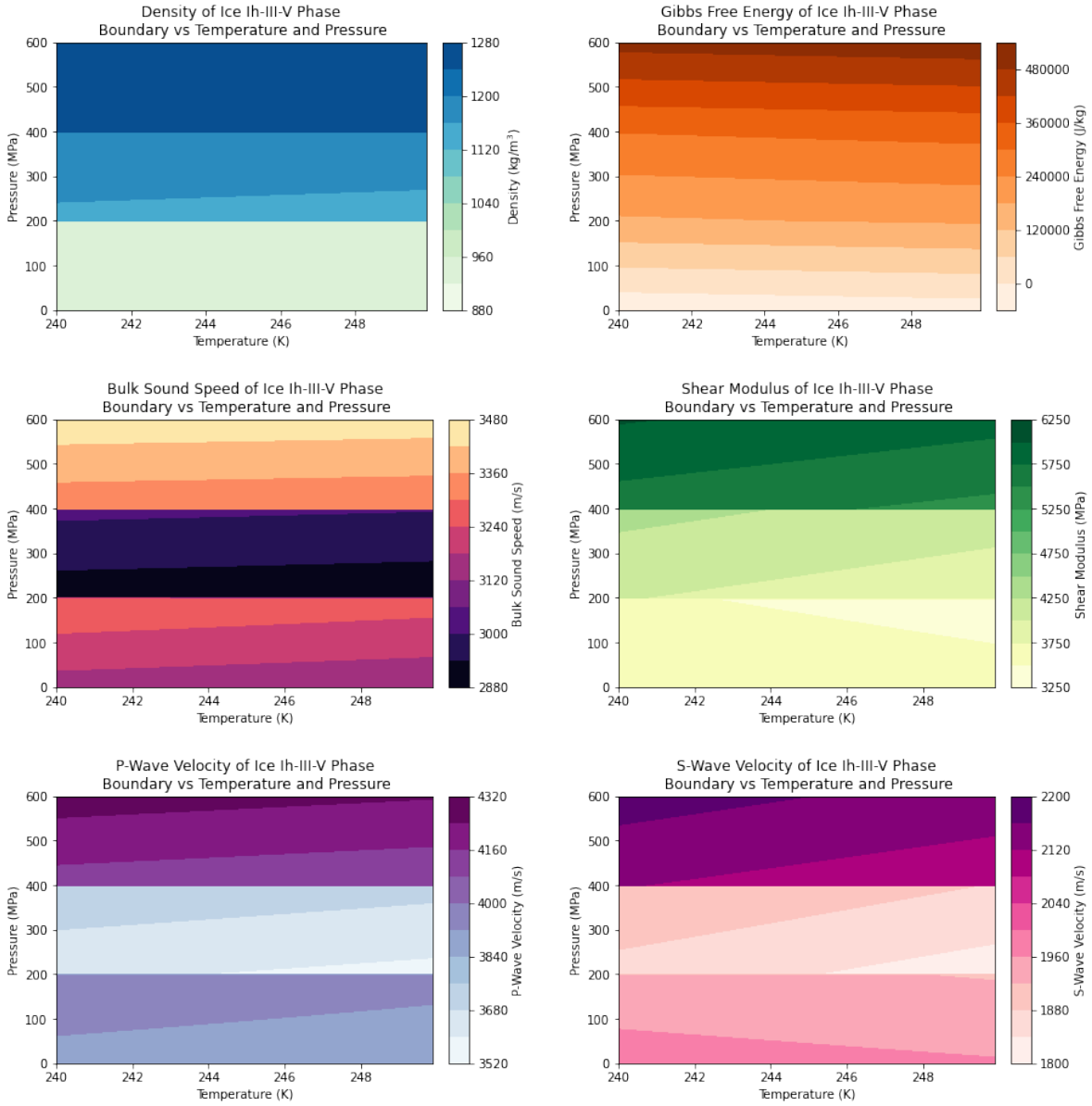

Figure 33: Thermodynamic properties across the solid-solid Ice Ih-Ice III and Ice III-Ice V phase boundaries plotted as functions of temperature and pressure.